RICE UNIVERSITY

Design and Construction of an Apparatus for Optically Pumping ^{87}Sr

by

Joshua C. Hill

A THESIS SUBMITTED
IN PARTIAL FULFILLMENT OF THE
REQUIREMENTS FOR THE DEGREE

Master of Science

APPROVED, THESIS COMMITTEE:

Dr. Thomas C. Killian, *Chair*
Professor of Physics and Astronomy

Dr. Junichiro Kono
Professor of Electrical and Computer Engineering, Professor of Physics and Astronomy

Dr. Kaden Hazzard
Professor of Physics and Astronomy

HOUSTON, TEXAS
AUGUST 2017

Rice University

Design and Construction of an Apparatus for Optically Pumping ^{87}Sr

by

Joshua C. Hill

A Thesis Submitted
in Partial Fulfillment of the
Requirements for the Degree

Master of Science

Approved, Thesis Committee:

Dr. Thomas C. Killian, *Chair*
Professor of Physics and Astronomy

Dr. Junichiro Kono
Professor of Electrical and Computer Engineering, Professor of Physics and Astronomy

---

Dr. Kaden Hazzard
Professor of Physics and Astronomy

Houston, Texas
August 2017

Abstract

Design and Construction of an Apparatus for Optically Pumping ^{87}Sr

by

Joshua C. Hill

The ability to control the population of ground-state magnetic sublevels in ultracold atomic gasses of fermionic ^{87}Sr is critical for experiments studying quantum magnetism in systems with many spin-components. This thesis describes the design and construction of hardware allowing the manipulation of spin populations via optical pumping. The apparatus operates using light scattering on the $^1S_0\,|F = 9/2, m_F\rangle \rightarrow {}^3P_1\,|F = 9/2, m'_F\rangle$ transition in strontium, near 689nm.

Acknowledgements

Thank you to everyone who has supported me, and sharpened my skills, along the unconventional path I took to graduate school. This includes (but is not limited to) my adviser Tom Killian, the other Killian lab graduate students, my family, professors at previous institutions, Valhalla, and Beta the fish.

To everyone who believes in me.

Contents

Abstract **ii**

Acknowledgements **iii**

1 Motivation **1**

1.1 Introduction 1

1.2 Spatial Periodicity 2

1.3 Why Strontium? 4

1.4 Spin Manipulation and this Thesis 5

1.5 Literature Survey: Cold, spin-polarized Sr and Yb 6

2 Background **9**

2.1 Strontium Basics 9

2.2 Singlets, Triplets, and Fine Structure 10

2.3 Hyperfine Structure 11

2.4 Zeeman Effect 14

3 Laser Trapping and Cooling **17**

3.1 Laser Trapping and Cooling 17

3.2 ^{87}Sr Trapping 24

3.3 Future Spin Polarization Sequence 26

4 Spin Manipulation **28**

4.1 Transition Probabilities 28

4.2 E1 Forbidden Transitions 30

4.3 Optical Pumping and Spin Polarization 31
4.4 Spin State Detection 33
4.5 Rabi Oscillations 36
4.6 Experimental Design Calculations 38

5 Experimental Particulars **42**
5.1 Hardware Overview 42
5.2 Cage System 44
5.3 461nm Blow-Away Beam 56

6 Conclusion **59**
6.1 Conclusion and Future Direction 59

References **60**

A Appendices **64**
A.1 Calculation of Hyperfine Parameters and g-factors 64
A.2 Optical Distances for OSG and Polarization Hardware 68
A.3 Blow-Away Machine Parts Drawings 70
A.4 Optical Pumping and OSG Machine Parts Drawings 74

List of Figures

1.1 Optical Lattice Depiction 3

2.1 Fine Structure Level Diagram 11
2.2 Full Level Structure 12
2.3 Hyperfine m_F Level Diagram 14

3.1 Repumping Spectroscopy 21
3.2 Hyperfine Structure and Detunings 26

4.1 Sigma and Pi Transitions 32
4.2 Linear Transition Level Diagram 33
4.3 Circular Transition Level Diagram 33
4.4 Zeeman Splitting of F = 9/2 sublevels 35
4.5 Rabi Frequency Example Data 38

5.1 Lattice Beam Propagation 44
5.2 Cage System for Optical Stern Gerlach and Spin Polarization 46
5.3 Cage System Schematic 47
5.4 Polarization Laser Path lengths 49
5.5 Cage System Closeup 51
5.6 Side View Of OSG Hardware 53
5.7 Top-Down View of OSG Hardware 54
5.8 Top View Of L-Bracket 55
5.9 Blow-away Beam Schematic 57
5.10 Side View of Blow-away Beam Hardware 58

List of Tables

1.1 Literature Survey 7

2.1 Sr Isotopes 9
2.2 Hyperfine Shifts 13
2.3 Hyperfine Zeeman Shifts 16

4.1 Experimental Parameters 40

5.1 Optical Lattice Beam Spot Sizes 44

A.1 Appendix Contents 64
A.2 Hyperfine-Isotope shifts and g-factor calculations 66
A.3 Optical Path-Length Changes 68
A.4 Polarization Optical distances 69
A.5 OSG Optical Distances 70

Chapter 1

Motivation

1.1 Introduction

Since its development in the late 1970s, laser trapping and cooling of dilute gasses has provided an exceptional tool for the study of fundamental atomic interactions [29]. As the experimental and theoretical techniques of the field matured, the community began increasing the complexity of the systems under study. This has taken many forms, from the cooling to quantum degeneracy of various atomic species, to directly cooling diatomic molecules [3]. The moniker of "ultracold" typically applies to atoms with temperatures less than a millikKelvin. At such temperatures, s-wave scattering becomes the dominant collision channel, and quantum mechanical effects begin to play an important role in the particle's motion. Today, ultracold atomic physics experiments are generating strong interest as testbeds for exploring the behavior of many interacting quantum particles. Given that the computational resources necessary to describe a collection of quantum particles increases exponentially with the number of constituents, the physics of such "many-body" systems is difficult to predict [4]. This challenge has initiated efforts to experimentally "simulate" many-body systems via the tools and techniques of cold-atom atomic physics, echoing ideas about

quantum computers Richard Feynnman put forth in the late 1980s [14]. The ubiquity of many-body systems in nature, particularly in condensed matter physics, provides an incentive for simulating their properties. Furthermore, when confined with strict spatial periodicity, certain laser-cooled atomic species have been predicted to display a "zoo" of interesting emergent many-body phases [9]. This hints at the possibility of discovering new physics, as well as extending existing condensed matter theories to better describe phenomena such as superconductivity.

1.2 Spatial Periodicity

Many materials of both practical and theoretical interest are crystalline in nature. This amounts to the electrons experiencing a periodic energy potential due to the to periodically arranged ionic centers. How electrons quantum mechanically tunnel between these potential energy wells, or lattice sites, and how multiple electrons occupying a single site interact, largely determine a material's electronic, magnetic, and thermal properties. Therefore there has been a growing interest in using cold, trapped, atoms as an electon-analogy. The aim of many cold-atom quantum-simulation experiments is to use a fermionic (half-integer spin) atomic isotope confined to a laser-generated periodic potential energy landscape, an optical lattice. Overlapping two counter-propagating laser beams of the same frequency creates a standing wave with stationary minima of the electric field. The field's interaction with neutral atoms will shift the quantized energy levels from their field-free values via the AC Stark effect. When the lattice laser's frequency is far smaller than any atomic energy level resonances (far "red-detuned"), the shifts make it energetically preferential for the atoms to occupy the periodic potential minima of the optical lattice [22]. The development of such optical lattices has provided experimental physicists with a powerful tool for simulating the environment that electrons experience within the ionic lattice of a

crystalline solid (e.g. tunneling and hopping between sites). As lasers can be quickly turned on and off, shifted in frequency, and manipulated precisely. This makes lasers an excellent means of controlling the depth, shape, and dimensionality (e.g. tubes, sheets, points) of the trapping potential. Optical lattices are also defect free, and can have disorder introduced in a controllable manner if the experimenter desires. Because of this they provide many opportunities for studying collective, many-body physics.

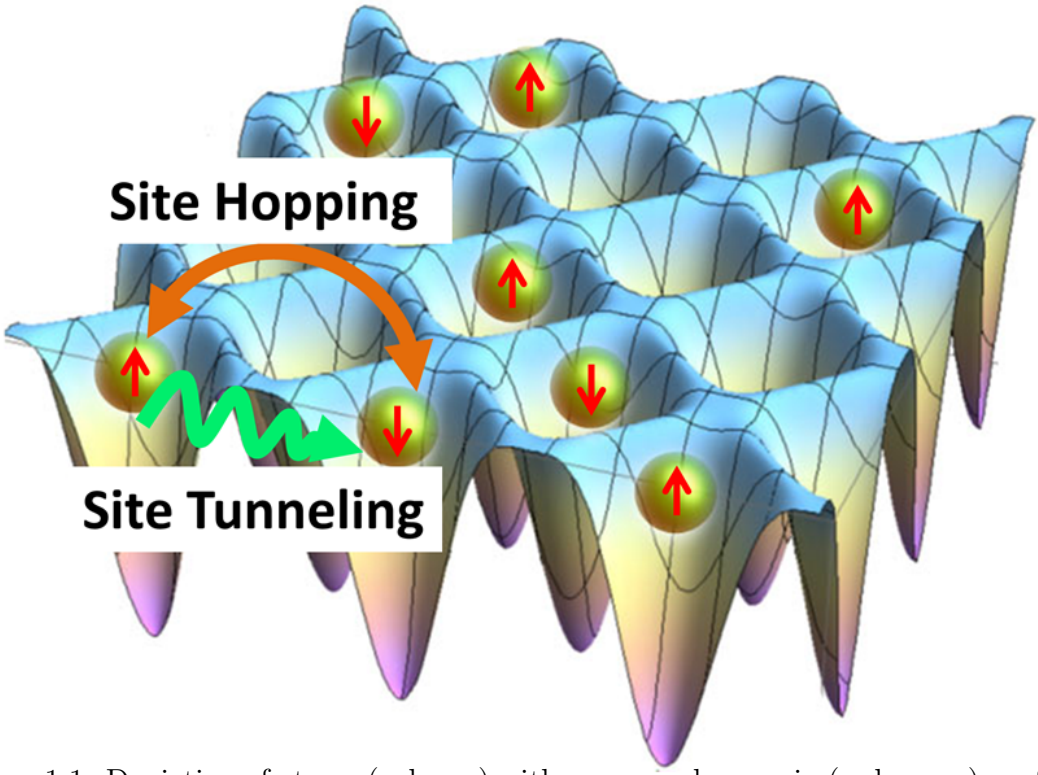

Figure 1.1: Depiction of atoms (spheres) with an up or down spin (red arrow) confined to a two-dimentional optical lattice. Two examples of the behavior of the atoms is depicted by the orange arrow (hopping over the potential barrier between sites) and the green arrow (tunneling through the barrier).

1.3 Why Strontium?

Out of the subset of elements for which conventional laser cooling is currently feasible, alkali metals such as rubidium and cesium have predominated in experiments. To date, most work studying many-body phenomena has been performed using such alkali metals. However, group-II elements such as strontium, and group-II-like elements (e.g. ytterbium) offer a different internal structure and are predicted to be a rich system for studying various types of magnetic ordering [9]. The internal structure of alkaline-earth metal atoms, with their paired valence electrons, offers a wide range of possible phenomena to study. The Killian lab works exclusivly with the alkaline-earth metal element strontium (Sr), and co-pioneered the creation of quantum degenerate samples of ^{84}Sr in 2009 [11] [32].

There are two primary properties making strontium's stable fermionic isotope (^{87}Sr) attractive for future quantum many-body physics experiments. First is the availability of a large number of degenerate magnetic m_f sublevels in the ground state. Second, the lack of electronic angular momentum in the ground state ($J = 0$), makes interactions between various $|F, m_F\rangle$ levels insensitive to spin-changing collisions. Here, F is the total atomic angular momentum quantum number, and m_F is the associated magnetic sublevel. This insensitivity isolates the m_f sublevels, and produces a symmetry in the interactions between the various N spin components (degrees of freedom. Stated more formally, the spin state symmetry available in ^{87}Sr allows for studying the physics of SU(N) symmetric systems. SU(N) is the group-theory designation for a particular type of symmetry, of degree N. In the case of ^{87}Sr with nuclear angular momentum quantum number of $I = 9/2$, $N = (2I + 1) = (2 \cdot \frac{9}{2} + 1) = 10$.

Numerous proposals for quantum-many-body simulation experiments take advantage of the above-described alkaline-earth element properties. These proposals in-

vestigate collective phenomena that manifest themselves as correlations between the spin states of atoms on different lattice sites. The proposals outline the possibility of using ultracold alkaline-earth atoms with many (N) symmetrically-interacting spin-components, trapped on an optical lattice as a way to explore the low temperature phases of certain theoretical models. The Fermi-Hubbard model is an example of one such model. Many of these models have been intensely studied for decades in attempts to explain high-temperature superconductivity, as well as other magnetic phenomena [18]. This is an active area of both theoretical and experimental research [21] [20].

1.4 Spin Manipulation and this Thesis

Once a sample of ^{87}Sr has been trapped and cooled with traditional techniques such as via a Zeeman slower and magneto-optical trap (MOT), the aforementioned experiments exploiting ^{87}Sr's spin-state symmetry require the relative populations of atoms in the various spin $|F, m_F\rangle$ states to be manipulated. This manipulation allows the researcher to create a particular mixture of spin states within a sample. Depending on the experiment to be performed, it may be desirable to spin-polarize the sample by putting all the atoms into a single $|F, m_F\rangle$ state, or to prepare a specific mixture. Therefore, spin manipulation is an essential component of many quantum-state-preparation routines, and a first step towards future experiments studying fermionic many-body physics in the Killian lab. In this thesis, I describe the design and construction of hardware that will allow optical pumping to manipulate various spin states, and describe the experimental groundwork for the implementation of more complex spin-manipulation techniques.

Optical pumping is the use of resonant light to transfer atoms into a specific quantum state or states. The states of interest here are various hyperfine $|F, m_F\rangle$

levels. Absorption of the photon's quantized energy promotes the atom into an excited energy state, from which it can then decay back down into a number of possible lower energy states. Using appropriately polarized light, and taking advantage of particular electronic energy-level arrangements, it is possible to alter the relative spin-state population. For example, it is also possible to collect atoms into a specific ground state when they decay. In this way, atoms are "pumped" into the desired state(s) after one or many excitation-deexcitation cycles. Development of the core ideas for this technique won A. Kastler the 1966 Nobel prize [1].

1.5 Literature Survey: Cold, spin-polarized Sr and Yb

Whether an atom is fermionic or bosonic is determined by the number of sub-atomic half-integer-spin particles of which it is comprised. An even number of electrons, neutrons and protons makes the atom bosonic, an odd number makes it fermionic. As the number of electrons and protons in neutral strontium remains fixed, the varying number of neutrons in the stable isotopes determine which statistics the atom follows. The only stable fermionic isotope of strontium is ^{87}Sr. In its $^1S_0$ ground state, Sr has a combined electronic angular momentum $\vec{J}$ (spin + orbital) of zero. ^{87}Sr posesses a nuclear angular momentum $I = 9/2$. Below I outline examples of other experimental groups spin polarizing laser-trapped samples of ultracold fermionic Sr atoms. Because it also possess two valence electrons and a similar electronic structure, I include information on a stable fermionic isotopes of Ytterbium, ^{173}Yb ($I = 5/2$). The above groups can be divided into two camps depending on their primary motivation for spin polarizing the atoms, though some labs are actively involved in both research areas. The first motivation is using spin polarized atoms for uncertainty reduction

Group P.I.	Location	Isotope(s)	References
J. Ye	U. Colorado, Boulder	^{87}Sr	[5], [27]
H. Katori	U. Tokyo	^{87}Sr	[2], [33]
F. Schreck	U. Innsbruck	^{87}Sr	[34], [31]
L. Fallani	U. Florence	^{173}Yb	[28], [8]
Y. Takahashi	U. Kyoto	^{173}Yb	[33], [16]
I. Bloch, S. Fölling	L.M.U. Munich	^{173}Yb	[30]

Table 1.1: Examples of other groups spin polarizing ultracold fermionic alkaline-earth or allkaline-earth-like gasses.

in precision timekeeping experiments (i.e. atomic clocks). To this end, the Ye and Katori groups have pumped atoms into the maximal $|m_F|$ "stretched states", then measured the states' resonance positions relative to each other to quantify shifts due to stray magnetic fields and collisional effects.

The other main motivation, and that most relevant to this thesis, is to prepare specific spin mixtures for studying the resulting many body effects. The Bloch, Schreck, and Fallini groups have all spin-polarized fermionic isotopes for this purpose. For instance, the Fallani group has used optical pumping to tune the number of spin states (N) present in one-dimensional chains of ^{173}Yb atoms. This allowed a systematic study of how the momentum distribution was dependent on N, and how the fermionic character of the gas can be altered [28].

Beginning with alkali-metals, and more recently in alkaline earth elements, the Optical Stern-Gerlach (OSG) technique has been used for spin-state resolved manipulation and detection. This technique exploits the varying line-strengths of differnt atomic transitions to apply a spin-state dependent force which can be used to spatially separate the various states the atoms have been pumped into. Once spatially seperated, the states can be imaged and quantified. The effect is an optical analog of the cannonical experiment in quantum mechanics where an inhomogeneous magnetic field was used to acheive the same result [17]. The optical version is particularly relevant to atoms with no electronic angular momentum such as the ground states of Sr

and Yb. In such isotopes, only the weak nuclear magnetic moment contributes to the overall moment, and impractically large field gradients would be required to separate the states purely magnetically [31]. The experiment hardware I have constructed for this thesis includes the components to allow for OSG to be implemented, though the focus here is spin polarization via optical pumping.

Chapter 2

Background

2.1 Strontium Basics

Of the four stable Sr isotopes, three are bosonic. This means they obey Bose quantum statistics. These isotopes have a total nuclear spin I of zero. Only ^{87}Sr is Fermionic, obeys Fermi quantum statistics, and possesses a nonzero ($I = 9/2$) nuclear spin.

Isotope	Natural Abundance (%)	Nuclear Spin $\lvert\vec{I}\rvert$	Governing Statistics
^{84}Sr	0.56	0	Bose
^{86}Sr	9.86	0	Bose
^{87}Sr	7.00	9/2	Fermi
^{88}Sr	82.58	0	Bose

Table 2.1: Basic properties of the four stable isotopes of Strontium.

The remainder of this thesis will be restricted to discussing ^{87}Sr. For a discussion of the other quantities in Strontium (e.g. oscillator strengths), see [35] and [10].

2.2 Singlets, Triplets, and Fine Structure

Strontium's two valence electrons can pair together in two different configurations, depending on the orientation of electron' spins. This orientation is indicated by arrows in the following equations. The electrons can either be in a singlet or triplet configuration, with the spins aligned antiparallel ($S = 0$) or parallel ($S = 1$) respectively.

$$S = 0, \text{Singlet} \begin{cases} \frac{1}{\sqrt{2}}(|\downarrow\uparrow\rangle - |\uparrow\downarrow\rangle \end{cases} \tag{2.1}$$

$$S = 1, \text{Triplet} \begin{cases} |\uparrow\uparrow\rangle \\ \frac{1}{\sqrt{2}}(|\downarrow\uparrow\rangle + |\uparrow\downarrow\rangle \\ |\downarrow\downarrow\rangle \end{cases} \tag{2.2}$$

The ground state is a singlet ${}^1S_0$ state. The excited states relevant for the optical pumping described in this thesis are the triplets, specifically the ${}^3P_1$ states. States are labeled by their quantum numbers in spectroscopic notation $\mathrm{n}^{2S+1}L_J$. The total electronic angular momentum is denoted by $\vec{J} = \vec{L} + \vec{S}$, the sum of the orbital and spin momenta. The various J that arise come from the vector addition rule are $J \in \{|L - S|, |L - S| + 1, \ldots, (L + S)\}$. For $L = 1$ and $S = 1$, as is the case here, $J \in \{0, 1, 2\}$. Spin-orbit ($\vec{L} \cdot \vec{S}$) coupling between the electron's orbital and spin angular momenta leads to an interaction that breaks the degeneracy of the various J states, splitting the triplet $5s5p\,{}^3P_J$ manifold. These fine structure energy shifts are on the order of $\alpha^4 m_e c^2$, where $\alpha = \frac{\mu_0 e^2 c}{4\pi\hbar}$ is the fine structure constant. Another important energy level for trapping and cooling strontium is the singlet ${}^1P_1$, depicted to the left alongside the triplet series in the figure below.

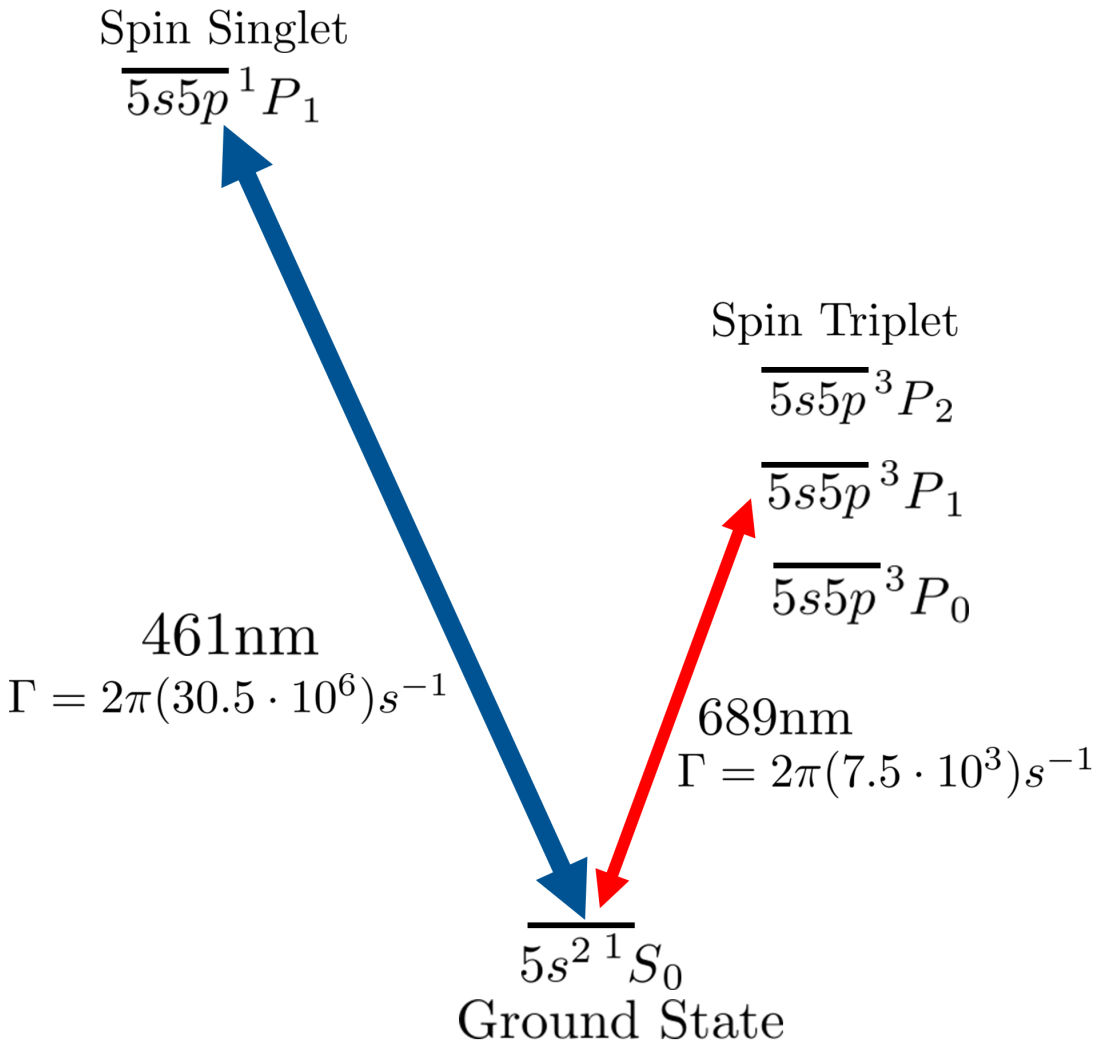

Figure 2.1: Enery-level diagram showing the basic transitions of interest for laser trapping and cooling of strontium, including the fine structure splitting of the triplet series.

2.3 Hyperfine Structure

The hyperfine atomic structure arises from a collection of effects, predominantly the nuclear magnetic moment's interaction with the magnetic field of the orbiting electron(s). Compared to fine structure splitting, the energy level shifts due to the hyper-

fine interaction are a factor of m_e/m_p smaller. Here $m_e/m_p \approx 1/2000$ is the electron to proton mass ratio.

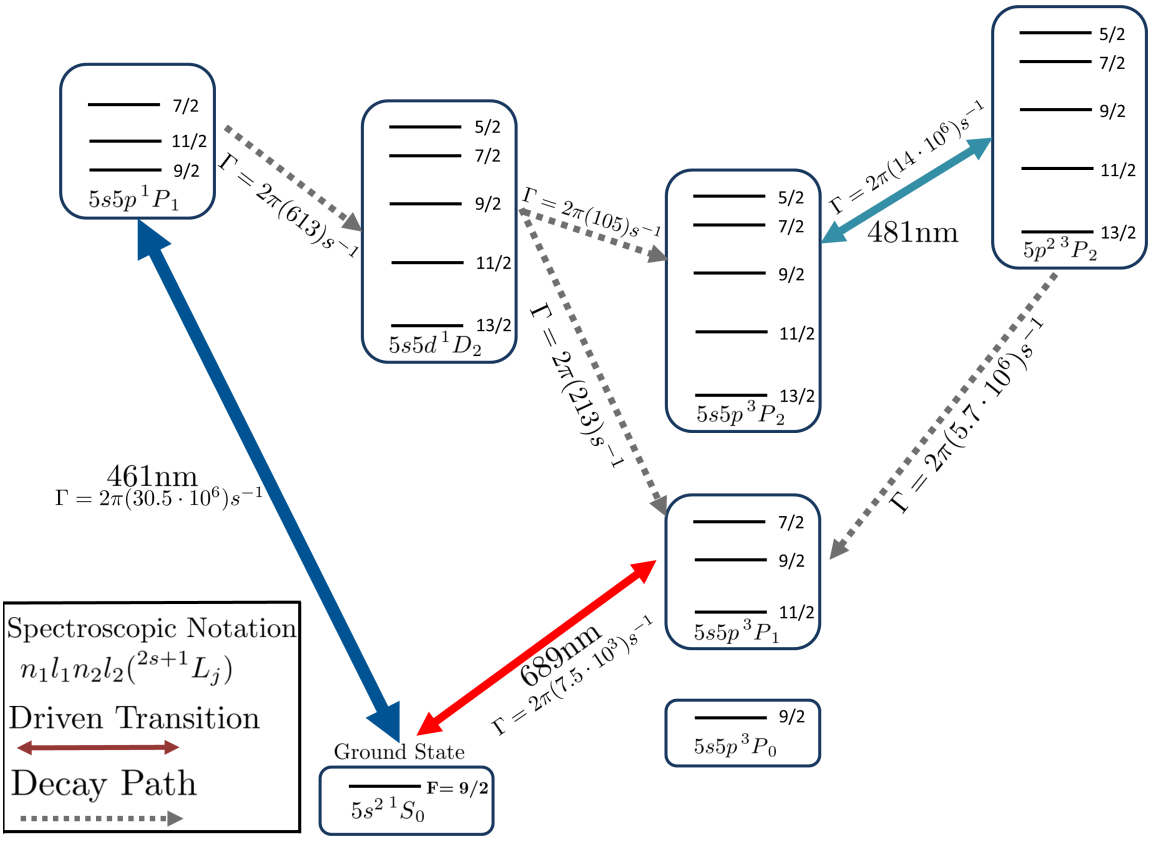

Figure 2.2: Full energy level diagram for the relevant low-energy states of ^{87}Sr. Shown here are the primary transitions of interest, as well as the hyperfine (F) states. The $2F+1$ magnetic m_F states are degenerate in the absence of a magnetic field, and are not shown. A transition's natural linewidth, or decay rate, is indicated by Γ. Solid lines are driven transitions, while dotted are spontaneous decays.

The $^1S_0$ ground state of strontium has zero electronic angular momentum ($J = L = S = 0$), and therefore no hyperfine structure. When combined with the $I = 9/2$ nuclear spin in ^{87}Sr, this leads to a total angular momentum quantum number $F = 9/2$ in the ground state. In the absence of an external magnetic field, the m_F

sub-levels are degenerate.

Contrary to the ground state, the Sr excited electronic states of interest here *do* posses a hyperfine structure. With $J = L = S = 1$ the $^3P_1$ manifold allows for possible hyperfine states possessing $F \in \{11/2, 7/2, 9/2\}$, as does the $S = 0$, $L = J = 1$ $^1P_1$ state. See the table below for the amount these levels shift from the same level in bosonic ^{88}Sr.

State	$^1P_1$ (MHz)	$^3P_1$ (MHz)
F=7/2	-9.7	1130.0
F=9/2	-68.9	222
F=11/2	-51.6	-1241

Table 2.2: Combination isotope-hyperfine shifts for ^{87}Sr. Second and third columns are the shifts of the transition going from the $^1S_0$ ground state, to the state indicated, *referenced to* ^{88}Sr. [7].

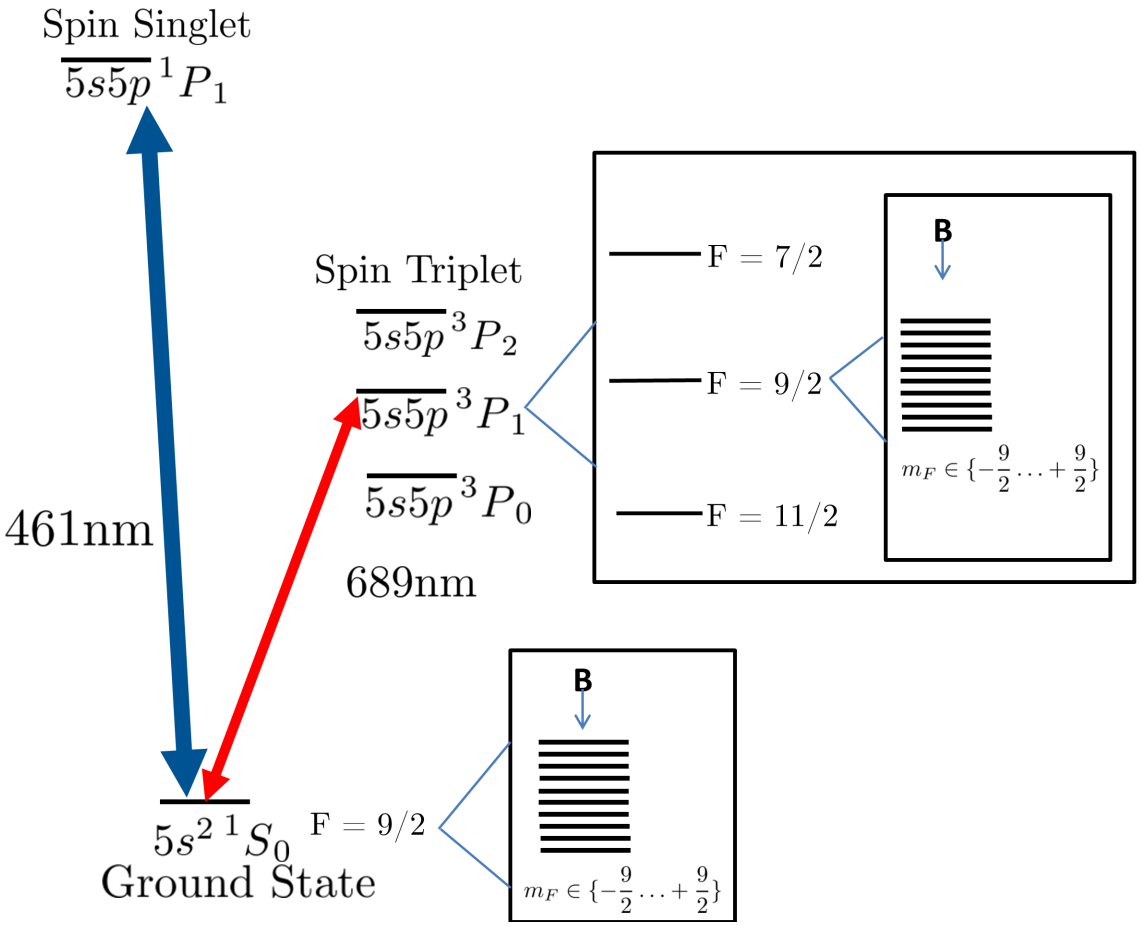

Figure 2.3: Energy level diagram for ^{87}Sr illustrating the ten m_F magnetic hyperfine states (with degeneracy split by a magnetic field **B**) in the ground and excited states of interest. The $^1P_1$ and $^3P_2$ states also posses hyperfine structure, which is not shown here.

2.4 Zeeman Effect

An atom's total magnetic moment is

$$\vec{\mu} = -\frac{\mu_B}{\hbar}(\vec{L} + 2\vec{S}) - \frac{\mu_N}{\hbar}\vec{I} \tag{2.3}$$

where the first term describes the contribution from electrons in the atom with orbital ($\vec{L}$) and spin ($\vec{S}$) angular momentum. The second term is the contribution from the nuclear angular momentum $\vec{I}$, where $\mu_N = e\hbar/(2m_p) = 5.051 \cdot 10^{-27}\text{J/T}$ is the nuclear magneton. However, because $\mu_N/\mu_B = \frac{m_p}{m_e} \approx 1800$, the nuclear contribution can typically be neglected for magnetic fields common in the laboratory.

The magnetic moment interacts with an external magnetic field $\vec{B}$ via

$$E = -\vec{\mu} \cdot \vec{B} \tag{2.4}$$

where the result is a torque $\vec{\tau}$ on $\vec{\mu}$ causing it to precess about the field, splitting the previously degenerate energy levels. Assuming that the field is sufficiently weak compared to the hyperfine interaction, the Zeeman effect can be treated as a small perturbation on top of the hyperfine interaction energy. In that case F and m_F are still good quantum numbers, and the Zeeman-shift in the energy varies linearly with respect to $\vec{B}$

$$E = \frac{g_F \mu_B B m_F}{\hbar} \tag{2.5}$$

breaking the degeneracy of the $2F + 1$ m_F levels, where g_F is the total g-factor (see appendix).

Note that because the nuclear moment is small, $J = 0$ states have a negligible shift due to the Zeeman effect. Despite this small contribution to the overall moment, the nuclear angular momentum being nonzero does critically create additional states (m_F). This insensitivity to magnetic fields motivates use of optical fields, versus magnetic fields, to apply forces to the different ground state m_F levels (e.g. optical Stern-Gerlach technique). Table 2.3 below contains calculations of useful Zeeman shift values for the ^{87}Sr $^1S_0 \rightarrow {}^3P_1$ transition of interest for optical pumping in this thesis.

F	g_F	$\frac{g_F\mu_B}{\hbar}$ (MHz/G)	$\lvert m_F\rvert$	$\frac{g_F\mu_B\lvert m_F\rvert}{\hbar}$ (MHz/G)	$\frac{\Delta E}{\hbar}$ (MHz)
7/2	-1/3	-0.466	7/2	-1.63	-3.27
			5/2	-1.17	-2.33
			3/2	-0.700	-1.40
			1/2	-0.233	-0.466
9/2	2/33	0.0848	9/2	0.382	0.764
			7/2	0.297	0.594
			5/2	0.212	0.424
			3/2	0.127	0.255
			1/2	0.0424	0.085
11/2	3/11	0.382	11/2	2.10	4.20
			9/2	1.72	3.44
			7/2	1.34	2.67
			5/2	0.955	1.91
			3/2	0.573	1.15
			1/2	0.191	0.382

Table 2.3: Selection of ^{87}Sr linear Zeeman shift parameters for the $^3P_1$ states. $\mu_B/\hbar =$ 1.4MHz/G is the Bohr magneton, and the final column assumes a magnetic field strength of 2 Gauss.

Chapter 3

Laser Trapping and Cooling

3.1 Laser Trapping and Cooling

As mentioned in the introduction, trapping and cooling atoms with lasers is a mature field, and an active research area. Here I will give a brief outline of the tools and techniques used in preparing cold atomic samples in this thesis. The existing apparatus used for trapping and cooling was built up by multiple generations of students. For more detail, see B. J. DeSalvo's thesis [12].

3.1.1 Precooling

The Sr atoms begin as solid metal (isotopes present in their natural abundances), which is then heated to about 700°C. They spew out of a nozzle and travel down a tube towards the main experimental chamber. Radial collimation and precooling are necessary, and these are the jobs of the 2D-collimator and Zeeman slower respectively. Lasers can cool atomic ensembles when atoms selectively absorb light from a beam opposing their motion. The selectivity can arise from the Doppler shift in the frequency of light a moving atom observes. This Doppler cooling underlies the

Zeeman slower, as red-detuned light counter-propagates against the incoming atomic beam. The incoming atoms are slowed as they absorb photons and are "kicked" by the associated momentum transfer. When the atoms spontaneously emit the energy, they do so in a random direction. Therefore re-emission is isotropic and adds no net velocity. However, as the atoms slow down, their Doppler shifted resonance changes. The Zeeman slower accounts for this change by including a magnetic field gradient along the tube to Zeeman-shift the levels back onto resonance with the laser, as they continue their forward travel.

3.1.2 Blue MOT

By this point the atoms have a sufficiently small velocity to be captured in a magneto-optical trap (MOT). MOTs are a staple in many-atom cooling labs, and use a combination of circularly polarized light and magnetic fields to provide both spatial confinement and velocity-dependent damping. For an introduction to the topic, I refer the reader to *Atomic Physics* by C. Foot [15].

In a typical MOT a qudrupole-magnetic-field gradient shifts the atomic resonances of the atoms as they move away from the center of the trap (region of zero field). The polarizations of the beams and orientation of the magnetic fields are arranged so that as an atom moves away from the center it scatters photons preferentially from the beam that pushes it back. Doppler cooling provides a force that damps the atom's motion. With six beams (three counter-propagating pairs), the MOT can cool and trap in all three spatial directions. This apparatus employs a two-stage MOT, utilizing both the broad linewidth ($\gamma = 30.5$MHz) ${}^1S_0 \rightarrow {}^1P_1$ ("blue" MOT), and narrow ($\gamma = 7.5$ kHz) ${}^1S_0 \rightarrow {}^3P_1$ ("red" MOT) transitions.

To begin, the blue (461nm) transition is used as its broad linewidth (short excited state lifetime) scatters many photons, quickly cooling the atoms and capturing

them from the incoming beam. The blue MOT achieves temperatures on order of a milliKelvin. This lower bound in temperature comes from the Doppler cooling limit, which imposes a minimum temperature (T_D) attainable with the Doppler cooling technique. The limit arises from the stochastic nature of photon emission and absorbtion, where each is accompanied by a momentum kick to the atom. While the recoil for spontaneous emission is isotropic and averages to zero, there is still a random walk in momentum space. This is a heating mechanism the reaches a balance with the cooling to produce a steady-state temperature. This temperature is dependent on laser parameters, and has a lower limit of $T_D = \hbar\gamma/(2k_B)$ where k_B is Boltzmann's constant. For the blue 461nm transition, $T_D = 732\mu$K. It is possible to cool below the Doppler limit in some particular configurations. However, as such sub-Doppler cooling is not expected to be exploited in the upcoming experiments this apparatus was designed for, I don't discuss it further.

3.1.3 Repumping

The primary loss channel from the blue ${}^1S_0 \leftrightarrow {}^1P_1$ cooling cycle is atoms decaying to the $(5s4d)\,{}^1D_2$ state, and from there to the metastable $(5s5p)\,{}^3P_2$ state with a probability of about 1×10^{-5} (1 out of 100,000) [23]. The long $(5s5p)\,{}^3P_2$ lifetime (20s with ambient blackbody radiation) prevents those atoms from returning to the ground state on an experimentally relevant timescale, and scattering additional cooling photons. To return these "shelved" atoms to the ground state where they can begin the cooling cycle anew, they are "repumped" up to the shorter-lived $(5p^2)\,{}^3P_2$ state via a 481nm laser. From there they decay to the $(5s5p^2)\,{}^3P_1$ state at a rate of $3.6 \cdot 10^7$ 1/s, and then back to the ground state. This is one of a few possible Sr repumping configurations, and is attractive because it requires only a single laser (Littrow-ECDL) and can benefit from a nearby tellurium line as a frequency refer-

ence. The repumping laser is locked by monitoring the transmission through the tellurium cell, exploiting a transition in tellurium conveniently only 50MHz from the natural-abundance isotope-averaged Sr repumping line.

Fortuitously, the $(5p^2)\,^3P_2$ state also has a magnetic moment and therefore contains magnetically trap-able low-field seeking m_F states. The quadrupole field of the blue MOT therefore doubles as a magnetic trap. To maximize the number of atoms captured, they are typically accumulated in the $(5p^2)\,^3P_2$ state ("loading the trap") before flashing on the repumper laser at the end of the blue MOT.

The hyperfine structure of ^{87}Sr adds additional lines to the $(5s5p)\,^3P_2 \rightarrow (5p^2)\,^3P_2$ repumper spectrum. To our knowledge, no data have been published on the HFS of this transition. At the time of writing this thesis we have begun exploring the various lines with the goal of mapping them, and possibly improving the repumping efficiency. The current repumping method used is to quickly (7kHz) sweep the repumper laser's frequency back and forth over the entire range of isotope-shifted resonances. This allows repumping different isotopes and improves ^{87}Sr repumping, though it means that the laser spends time in "dead-zones", off-resonant for any transition. Shown below are the preliminary results of repumping spectroscopy on all the Strontium isotopes, and tentative line assignments for the ^{87}Sr lines.

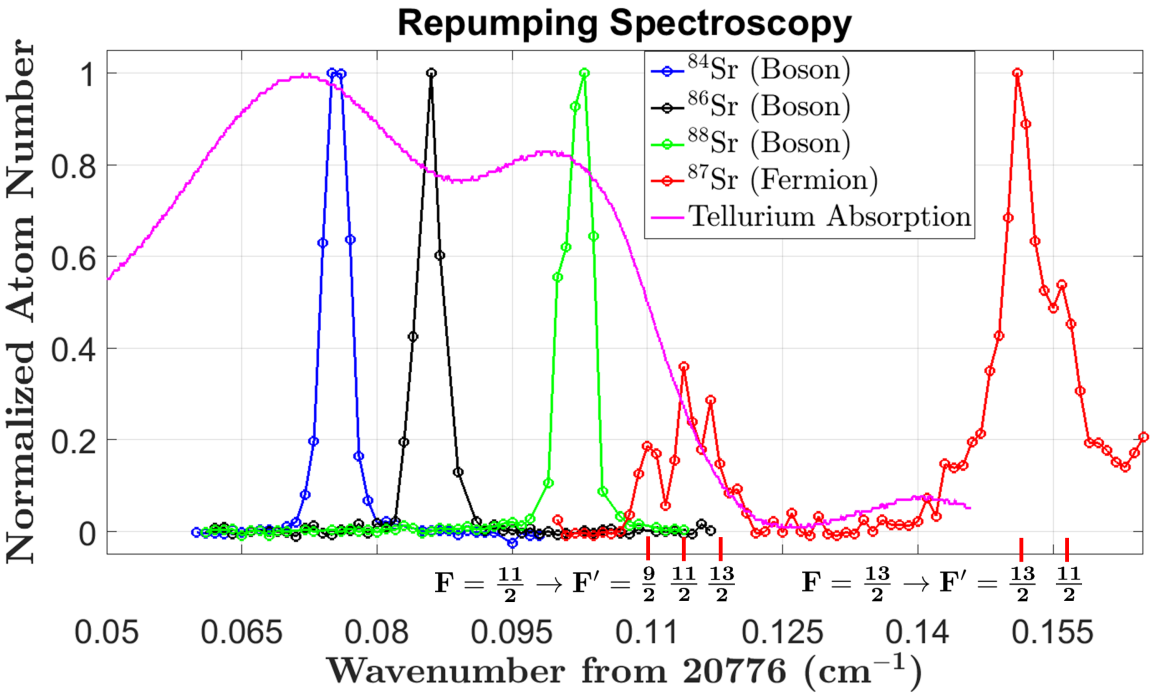

Figure 3.1: May 2017 repumping Spectroscopy on the $(5s5p)\,^3P_2 \rightarrow (5p^2)\,^3P_2$ line for the various Strontium isotopes. ^{87}Sr line assignments are tentative, pending more data.

3.1.4 Red MOT

The blue MOT is effective for capturing many atoms from the Zeeman-slowed beam, however, to get even colder, Sr's intercombination (689nm) transition is exploited in a second-stage red MOT. A MOT operating on such a narrow $\gamma = 7.5$kHz line can be characterized by the ratio of the linewidth (γ) to the recoil frequency $\omega_r = (\hbar k^2)/(2m)$, with k the light's wavevector magnitude [24]. For the $^1S_0 \rightarrow {}^3P_1$ transition $\gamma/\omega_r = 1.6$, vs the $\Gamma/\omega_r \gg 1$ for traditional broad-line MOTs. The 0.180μK Doppler temperature for this transition is three orders of magnitude lower than it's blue counterpart, and temperatures of about a microKelvin are routinely achieved in the red MOT.

Because of its narrow linewidth, the red transition interacts only with a small

subset of atoms with velocities in a particular range (velocity "class"). In order to efficiently capture atoms from the blue MOT, the red MOT beams are artificially frequency-broadened by modulating the driving frequency of an acousto-optic modulator that the beams pass though. Thereafter the modulation amplitude can be reduced, and the frequency spread narrowed down to further cool the atoms.

Fermionic ^{87}Sr's hyperfine structure introduces some unique challenges for the red MOT compared to the Bosonic isotopes. In particular, the g factor of the $^3P_1$ excited state (g_e) is much larger than that of the purely nuclear $^1S_0$ ground state (g_g). This imbalance causes the differential Zeeman shift of each transition to be substantially different, versus the essentially commensurate levels shifts for the case of atoms with ($g_e/g_e \approx 1$). Commensurate level shifts allow the $\sigma_\pm$ polarized MOT lasers to maintain a common detuning from all the possible transitions independent of the atom's location in the trap. However, transitions excited from ^{87}Sr's ten magnetic ground levels can be shifted to either side of resonance with respect to the laser. This spatial dependence to the sign of the transition detuning introduces challenges to trapping the atoms, depending on the combination of the atom's location in the trap and quantum state. For example, an atom can get into an unlucky combination of location and state such that it is anti-trapped, or resonant with a transition that kicks the atom *away* from the trap center. In the bosonic Sr isotopes, the single magnetic ground state did not introduce any such complexity.

Fortunately, the MOT light also optically pumps atoms into states with transition probabilities (related to the Clebsh-Gordon coefficients) that favor trapping over anti-trapping or off-resonant transitions. This results in a net trapping force. The Clebsh-Gordon coefficients for $F = 9/2 \rightarrow F' = 11/2$ transitions increase with more positive m_F for σ_+ and more negative m_F for σ_-. Therefore, stretched states for which $m_F = \pm F$ offer the highest probability for receiving restorative trapping photon-

kicks, vs repulsive anti-trapping ones. Thus, optical pumping that occurs naturally in the MOT's circularly polarized beams aids the position-dependent Zeeman level shifts in providing a net restoring force towards the trap center [6].

For the broad linewidth 461nm MOT, this optical pumping and operation red-detuned of the hyperfine levels ensure stable operation. However the narrow linewidth of the 689nm MOT means the atoms have a narrow spatial region (a shell) where the field will be appropriate to shift them onto resonance. Just a few photon kicks can move them out of this region, and therefore the cooling cycle. To ensure stable operation of the red MOT, in addition to the trapping beams operating close to the $|F = 9/2, m_F\rangle \rightarrow |11/2, m_F\rangle$ resonance, a "stir" beams near the $|F = 9/2, m_F\rangle \rightarrow |9/2, m_F\rangle$ transition frequency is also used. The upper level of the stir transition has a weaker magnetic field dependence than that of the upper level in the trapping transition, by a factor of $g_{11/2}/g_{9/2} = 4.5$. This allows the stir beams to stay on resonance with the atoms longer, scattering light from a larger volume shell within the trap. The longer interaction time allows for a quicker mixing of populations between the various ground m_F states than with the trapping beams alone, ensuring that the average restoring force is achieved. For more intormation about the specifics of a ^{87}Sr red MOT, the reader is referred to the seminal paper by the Katori group [26].

3.1.5 Optical Dipole Trap

After the MOT stages, the atoms are typically loaded into an optical dipole trap (ODT). Operating at a wavelength of 1064nm, the ODT is far-detuned from any atomic transitions of interest and traps atoms via the gradient force, or optical dipole force. Neutral particles under illumination by laser light develop an induced, oscillating, electric dipole moment. This moment interacts with the light's electric field

to shift the particle's (e.g. atom's) energy levels. This light-shift, or AC Stark shift, makes it energetically preferential for atoms *in the ground* state to move to regions of *higher* beam intensity, when the beam is detuned red of any atomic transisitons of interest. For a good review of the topic, see reference [19]. Considering a laser beam with a Gaussian cross section profile, as is typical in the lab, the light-force pushes atoms inward radially, towards the beam center. Unless the Rayleigh length of the beam is very short, this force does not provide appreciable axial confinement, thus a pair of crossed beams is used.

The ODT is an effective means of trapping the atoms pre-cooled by the MOTs. It also provides another cooling procedure when the ODT laser intensity is reduced over time, lowering the trapping potential experienced by the atoms. Such forced evaporative cooling allows the most energetic atoms to escape, lowering the average temperature of the remaining sample. This is typically the final step in routines for creating Bose-Einstein condensates (BECs) and degenerate Fermi gasses.

3.2 ^{87}Sr Trapping

Although this apparatus has trapped ^{87}Sr in the past, the inevitable changes in equipment and procedures since then made it necessary to explore and optimize the trapping parameters again [13]. This was a multi-faceted problem with a large parameter space. There are many "knobs" available for tweaking to try and maximize the number of ^{87}Sr atoms captured, and to minimize their temperature. The blue MOT has a normal duration of operation, as well as a "cold" phase where the power is reduced and other parameters altered. The red MOT has both broadband and narrowband phases. As well as the duration of each phase, the individual stages have variable intensities, magnetic field gradients, and trapping frequencies. In the case of the red MOT, the number of parameters is doubled as the trap *and* stir beams have inde-

pendent controls. Once the atoms are cold enough ($T \approx 1\mu K$), they can be loaded into the ODT and evaporativly cooled. The way the ODT laser power is lowered as a function of time is called the evaporation "trajectory" and is another potential item to optimize.

These parameters and their combinations were systematically explored until sufficient results were obtained for the optical pumping experiments the hardware in this thesis was constructed to perform. By the end of the red MOT approximately six million ^{87}Sr atoms were routinely trapped. This atom number includes the factor of two over the number reported by the computer fit program. Optical pumping effects are the reason only half of the ^{87}Sr atoms are imaged, and subsequently reported by the program [25]. As verified by fitting the cloud radius at multiple drop times, these six million atoms had reached a temperature of about $2\mu K$ at the end of the narrowband red MOT.

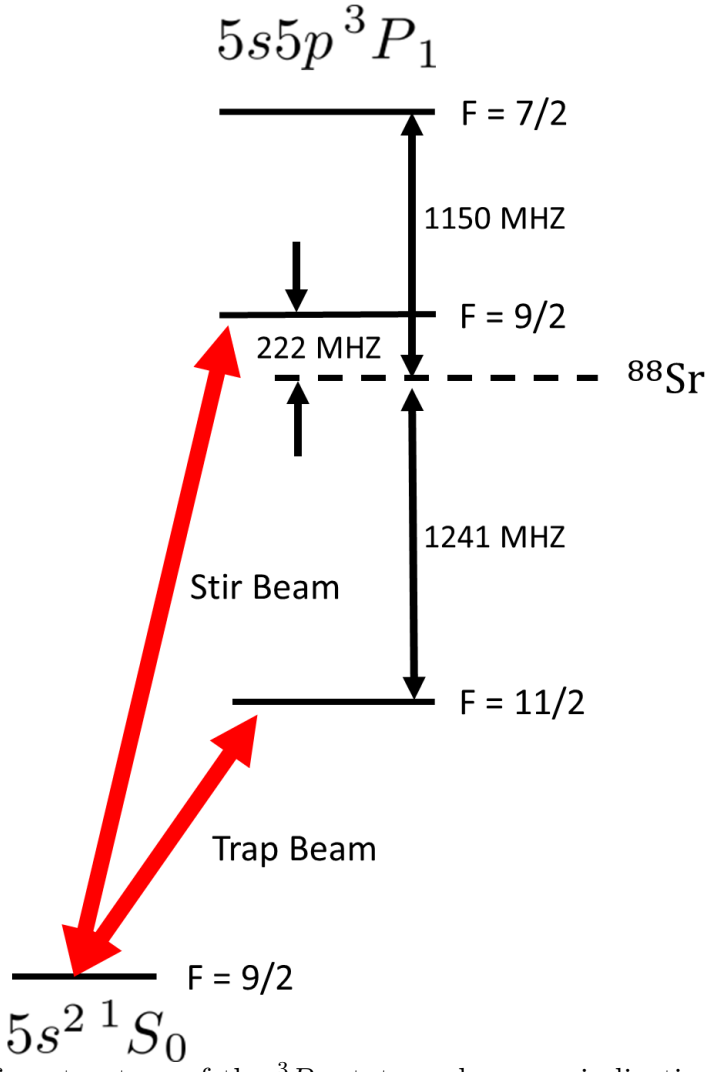

Figure 3.2: Hyperfine structure of the $^3P_1$ state and arrows indicating the stir and trap transitions used in the operation of the red MOT. The shifts from ^{87}Sr $^3P_1$ state (dashed line) are indicated. Prior to beginning their ramps closer to resonance, both the stir and trap beams are detuned -1.2MHz from the respective hyperfine levels.

3.3 Future Spin Polarization Sequence

Optical pumping will be performed by directing the 689nm light onto the atoms after loading them into the ODT. The red MOT beams will be extinguished prior to the polarization light being turned on to avoid interfering with the optical pumping

process. The atoms will be polarized prior to evaporative cooling to mitigate trap losses induced by light-assisted collisions by the near-resonant light at high atom-densities. The sample's spin population distribution can then be studied in various ways, as described in chapter four.

Chapter 4

Spin Manipulation

This chapter will discuss the basics of the energy transitions important to optical pumping. The chapter will also motivate the discussion by addressing how calculations informed the design choices of experimental hardware and parameters. The hardware will be used to alter the spin population of the atomic sample via the scattering of photons via optical pumping, then detect the resulting spin imbalance. Under the appropriate experimental conditions, this can be achieved by taking advantage of state-dependent atomic probabilities for absorption and emission.

4.1 Transition Probabilities

Determining when an atom under illumination will transition between various energy states is the purview of any graduate-level quantum mechanics textbook such as J. J. Sakurai's "Modern Quantum Mechanics". For spin polarizing strontium into different $|\beta, F, m_F\rangle$ states, it is important to know how the rules of quantum mechanics favor particular transitions, and with what probabilities. When the wavelength (λ) of light with wavevector $k = \frac{2\pi}{\lambda}$ is much larger than the size of the emitting or absorbing atom, the electric dipole approximation (E1) is valid. Within this approximation

$k \cdot (r_{atom}) \ll 1$ and $e^{i\vec{k}\cdot\vec{r}} \approx 1$. The electric field polarization vector is $\vec{\epsilon} = \epsilon_x\hat{x} + \epsilon_y\hat{y} + \epsilon_z\hat{z}$. An atom's absorption cross section for a particular two-level transition $|\beta, F, m_F\rangle \rightarrow |\beta', F', m'_F\rangle$ broadened by it's natural linewidth Γ is

$$\sigma_{\beta F m_F \rightarrow \beta' F' m'_F}(\omega) = \frac{2\pi\alpha\omega\Gamma}{(\omega - \omega_0)^2 + (\Gamma/2)^2} \left| \langle \beta, F, m_F | \, \hat{\epsilon} \cdot \hat{r} \, | \beta', F', m'_F \rangle \right|^2 \tag{4.1}$$

where ω is the light's angular frequency, α is the fine structure constant, $\omega_0 = \omega_i - \omega_f$ is the frequency difference between the two states, β is a collection of quantum numbers, and $\hat{r}$ is the position operator.

Typically, the most difficult part of calculating the cross section is the transition dipole matrix element $\langle \beta, F, m_F | \, \hat{\epsilon} \cdot \hat{r} \, | \beta', F', m'_F \rangle$. The work is simplified considerably if the Wigner-Eckart theorem is employed. Given two states of angular momenta F and F', and a spherical tensor operator $T_q^{(\kappa)}$, the theorem allows separation of the matrix element into a product of two terms. Mathematically, the theorem states

$$\langle \beta, F, m_F | \, T_q^{(\kappa)} \, | \beta', F', m'_F \rangle = \langle \beta, F | \, |\hat{r}| \, | \beta', F' \rangle \begin{pmatrix} F & \kappa & F' \\ -m_F & q & m'_F \end{pmatrix} \tag{4.2}$$

The first factor on the right hand side, the reduced matrix element, describes the dynamics and has no m_F dependence. The geometry of the configuration is described in the second term, the Wigner 3-j constant within the parentheses.

The tensor operator for calculating the absorption cross section is $\hat{\epsilon} \cdot \hat{r}$. This is of rank one, so $\kappa = 1$. Depending on the polarization state of the incident light, the angular momentum transferred to the atom is set by q, with $q = \pm 1$ for $\sigma_\pm$ and $q = 0$ for π.

Applying the Wigner-Eckart theorem to the matrix element in the absorption

cross section equation gives

$$\sigma_{\beta F m_F \to \beta' F' m'_F}(\omega) = \frac{2\pi\alpha\omega\Gamma}{(\omega-\omega_0)^2+(\Gamma/2)^2} \mid \langle \beta, F \mid \mid \hat{r} \mid \mid \beta', F' \rangle \mid^2 \sum_q |\epsilon_q|^2 \begin{pmatrix} F & 1 & F' \\ -m_F & q & m'_F \end{pmatrix}^2 \tag{4.3}$$

where ϵ_q are the projections of the polarization vector $\hat{\epsilon}$ along the spherical tensor components. The Wigner 3-j constant (or "symbol") can be related to the Clebsh-Gordon (CG) coefficients $C^{F,1,F'}_{-m_F,q,m'_F}$ as follows.

$$\begin{pmatrix} F & 1 & F' \\ -m_F & q & m'_F \end{pmatrix} = \frac{(-1)^{F-1-m'_F}}{\sqrt{2F'+1}} C^{F,1,F'}_{-m_F,q,m'_F} \tag{4.4}$$

Note that the 3-j symbol vanishes unless $q+m = m'$. The combination of this with the rules for addition of angular momenta forms a powerful simplification when finding the matrix elements between many different m_F states. It dramatically reduces the number of calculations required. The reduced matrix element becomes a common proportionality factor that only has to be calculated once, while the CG coefficients are readily available in tables, or from computer programs. Selection rules describing which transitions between states can occur arise from this, as do relative transition probabilities via calculating the square of the non-vanishing CG coefficients.

4.2 E1 Forbidden Transitions

The electric dipole, or $E1$, selection rules govern which transitions between energy levels may occur, and follow directly from a calculation of the matrix elements. $\Delta S = 1$ transitions are forbidden, because the light field does not couple to spin, changing only the orbital angular momentum l and it's projection m_l. For Sr, mixing of singlet and triplet levels means that $\Delta S = 1$ transitions can weakly occur. In heavy atoms

the $\vec{L} \cdot \vec{S}$ coupling picture begins to break down, and atomic states are mixtures of pure singlet and triplet configurations. Thus the "intercombination" ${}^1S_0 \rightarrow {}^3P_{\{0,1,2\}}$ $\lambda \approx 689$nm transitions can occur, albeit with narrow linewidths. These narrow linewidths (conversely, long lifetime or metastable excited states) are advantageous for a number of applications including laser cooling the atoms and precision spectroscopy. The decay rate of the ${}^3P_1$ state to ground is $\Gamma = 2\pi(7.5 \times 10^3)s^{-1}$, therefore the linewidth of the ${}^3P_1 \rightarrow {}^1S_0$ is $\gamma = 7.5$kHz. The spacing between different J manifolds are sufficiently large that we can focus on only one at a time, here the $J = 1$, $F = \{7/2, 9/2, 11/2\}$ manifold. See figure 2.1 and table 2.2. It is this ${}^1S_0(F = 9/2) \rightarrow {}^3P_1(F = 9/2)$ transition that future experiments will use for optically pumping the ground state atoms into the ten possible $m_F = -9/2 \ldots + 9/2$ states.

4.3 Optical Pumping and Spin Polarization

The spin polarization stage will occur just after loading the atoms into an optical dipole trap (ODT). Optical pumping occurs during normal red MOT operation, and it has been shown empirically that this pumping leads to a roughly equal population distribution of the ground m_F states amongst the ten available levels [13]. This is the unpolarized state prior to spin polarization.

The selection rules mentioned above, specifically that $\Delta m_F = 0, \pm 1$, can be taken advantage of to alter the populations of the m_F states. With this rule the polarization state of the excitation laser, as well as it's propagation direction, determines which transitions occur and their relative probabilities. Choosing a quantization axis $+\vec{z}$ along the direction of an applied magnetic field $\vec{B}$, pure $\sigma_\pm$ polarized light drives $\Delta m_F = \pm 1$ transitions, and the polarization vector ($\vec{E}$ direction) lies in the x-y plane. π polarized light drives $\Delta m_F = 0$ transitions, and the polarization is parallel to $\vec{z}$. When the light propagates in the $+\vec{z}$ direction, σ_+ polarization corresponds

to right-circularly polarized light. Changing the propagation direction to $-\vec{z}$ would correspond to left-circularly polarized. For light to have pure π polarization it must propagate in the x-y plane.

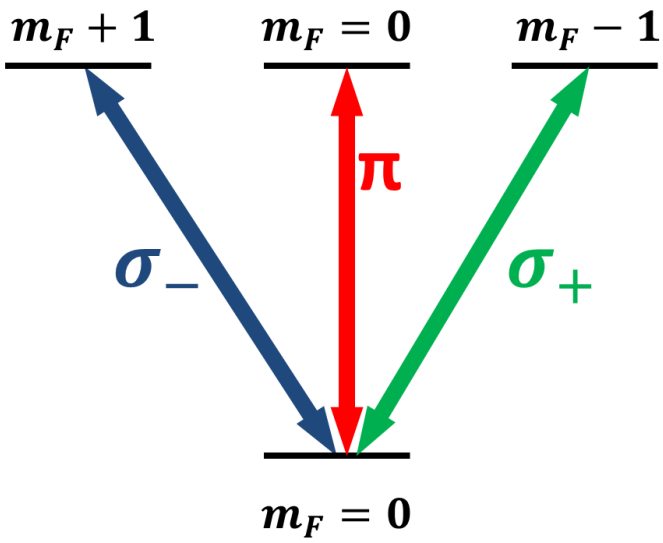

Figure 4.1: Depiction of $\sigma_\pm$ and π transitions.

Applying σ_+ light of the appropriate frequency will therefore drive atoms into higher m_F states, assuming such states exist. Excited states can decay back down into multiple levels, subject only to the $\Delta m_F = \{0, \pm 1\}$ selection rule, and with probabilities proportional to the Clebsch-Gordon coefficients. Decaying to the ground state initiates the cycle once more. However, eventually the atom will reach the maximal m_F, or stretched, states in the ground F manifold. Assuming the light is coupling a ground and excited state of the same F, e.g. ${}^1S_0(F = 9/2) \rightarrow {}^3P_1(F = 9/2)$, electrons will remain in the stretched state and cease to scatter photons. This is because in this configuration the $+m_F$ stretched state is "dark" to σ_+ circularly polarized light. Atoms in this state cannot absorb the light as there is no higher $m_F = +1$ state to be excited to. Thus after a sufficient number of photon scatterings, the atom will be "pumped" into the stretched state. Applying σ_- light will pump

atoms in the opposite direction of what was just described.

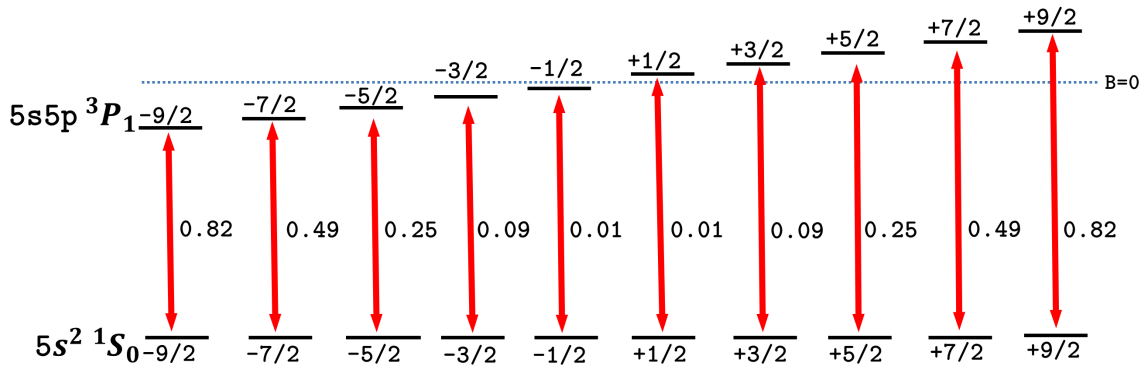

Figure 4.2: $F = 9/2 \rightarrow F = 9/2$, π transitions. Numbers to the right of the transitions are the square of the Clebsch-Gordon coefficient, from [25].

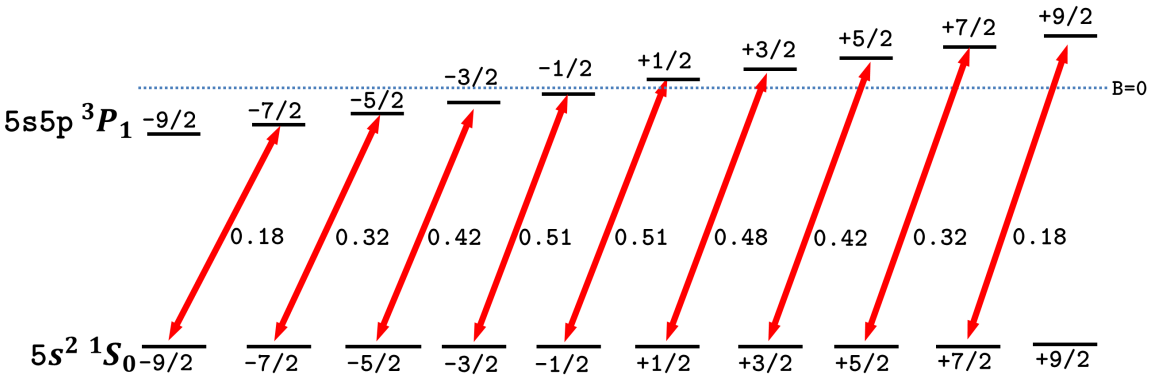

Figure 4.3: $F = 9/2 \rightarrow F = 9/2$, σ_+ transitions. Numbers to the right of the transitions are the square of the Clebsch-Gordon coefficient, from [25]. For σ_- transitions the CG coefficients would be mirrored to the left.

4.4 Spin State Detection

There are various ways to resolve and detect the populations of individual m_F states to provide evidence for spin polarization. As mentioned in the introduction, the optical Stern-Gerlach technique of spatially separating the clouds corresponding to different magnetic sublevels is a possibility [31]. The work done in this thesis lays

the groundwork for implementing the OSG technique in addition to optical pumping. However, as the OSG technique is another step removed from the polarization experiments this thesis' hardware is primarily focused on, it is not discussed further.

Once ^{87}Sr atoms are spin polarized, there are two methods planned to provide evidence that spin polarization has been achieved. The first method is spectroscopy. A magnetic field can be applied to separate (Zeeman shift) the upper energy levels, and a 689nm beam used to excite atoms to a specific level. Any atoms remaining in the ground state can then be removed from the trap via a 461nm blow-away beam pulse (see chapter five for details). This blow-away occurs sufficiently quickly that the excited atoms are still "shelved" in the higher-energy metastable state. Knowing the frequency of the excitation laser, the calculated Zeeman splitting of the states, and the number of atoms detected after the blow-away pulse, provides evidence for the number of atoms excited to the various $^3P_1$ $|F = 9/2, m_F\rangle$ levels. The frequency of the 689nm laser can then be scanned over a range that encompasses the shifted states, to map out their positions in frequency space. The Zeeman splitting of the various levels of interest for optical pumping in this thesis are plotted below over a range of experimentally accessible magnetic fields.

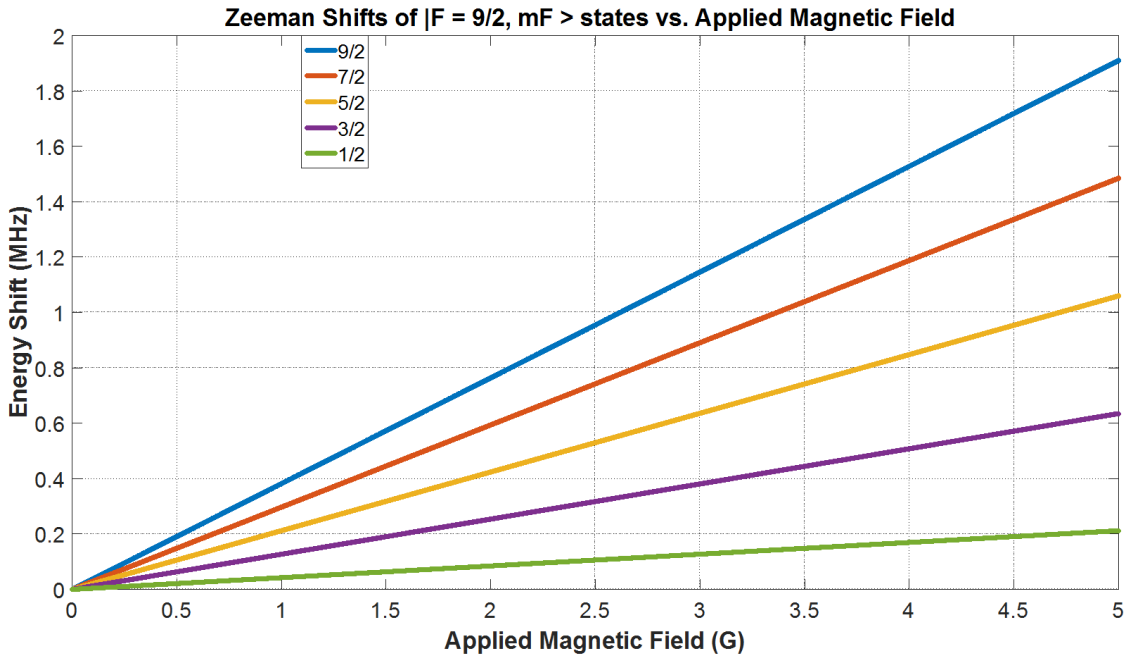

Figure 4.4: Zeeman shifts of the $|F = 9/2, m_F\rangle$ levels. Note that the negative m_F levels (not shown) have the same magnitude splitting away from zero, but mirrored about the the horizontal axis.

The second detection method is unforced evaporation in the ODT, where the sample is held in a static optical potential, and the hottest (most energetic) atoms escape [25]. The collisional properties of the gas are altered as it becomes more, or less, spin polarized. Thus it is possible to observe the rate of unforced evaporation for various samples to observe how quickly the atom number and temperature decrease with time. As the atoms have already been loaded into the ODT, they are at a temperature of approximately 1μK. At this low temperature, the only collissions energetically allowed are s-wave collissions. Identical (indistinguishable) fermions in the same internal state are forbidden from colliding because the total wavefunction must be antisymmetric with respect to partical exchange. Therefore, a perfectly spin polarized sample (single m_F component) will behave more like ^{88}Sr with its small background scattering length of $a_{88} = -1.4 \cdot a_0$ and evaporate down in temperature

more slowly than that of unpolarized ^{87}Sr ($a_{87} = +96.2 \cdot a_0$) [25]. The Bohr radius is denoted as a_0.

4.5 Rabi Oscillations

Physical access to beams at the location of the atoms is typically not possible due to the atom's being confined within an ultrahigh vacuum (UHV) chamber. However, the in-situ conditions the atoms experience is important to quantify. Therefore, observing the frequency of Rabi oscillations between quantum states is a useful tool for determining the beam intensity. It also allows tests of how long a sample can maintain coherence before the oscillations damp out.

When the frequency ω of coherent light is close to the resonant frequency ω_0 of an atomic transition the rotating-wave approximation can be used. Employing this approximation, and assuming a two-level atom which starts in the ground state such that the probability amplitude $|c_g(0)|^2 = 1$, the solution to the associated time-dependent Shrödinger equation shows that the probability oscillates between the two levels at a characteristic Rabi frequency Ω_R. On resonance such that $\omega = \omega_0$, the the excited state occupation probability goes as

$$|c_e(t)|^2 = sin^2\left(\frac{\Omega_R t}{2}\right) \tag{4.5}$$

The key factor resulting in these oscillations is quantum coherence between the states. Decoherence due to spontaneous emission is called radiative damping. Various other linewidth-broadening phenomena such as Doppler broadening, or stray magnetic fields also cause decoherences. Assuming sufficiently long illumination, the atom population settles down to a constant value. If N_1, N_2 are the state populations

($N = N_1 + N_2$), and I is the beam intensity, then

$$N_1 - N_2 = \frac{N}{1 + I/I_{sat}} \tag{4.6}$$

The saturation intensity I_{sat} of a transition with wavelength λ and linewidth Γ is defined (as in [15]) as

$$I_{sat} = \frac{\pi h c \Gamma}{3\lambda^3} \tag{4.7}$$

This is conveniently related to the Rabi frequency via

$$\Omega_R = \Gamma \sqrt{\frac{I}{2I_{sat}}} \tag{4.8}$$

For the ${}^1S_0 \rightarrow {}^3P_1$ transition, $I_{sat} = 3\mu\text{W/cm}^2$. To compare, for the broad ${}^1S_0 \rightarrow {}^1P_1$ transition, $I_{sat} = 40.7\text{mW/cm}^2$

The plot below shows an example of such data in ^{86}Sr. In it, the atoms were imaged after forced evaporation in the ODT and 29ms of ballistic expansion. The horizontal axis is the duration of a 20μW 689nm pulse from 2.5μs to 40μs. The vertical axis is the number of atoms imaged after an 0.8μs 461nm blow-away pulse. The data are fit to the optical Bloch-equations (OBEs) and the excited state density matrix element ρ_{ee} is plotted. These data and the fit show an extracted Rabi frequency of $\Omega_R/(2\pi)$=262kHz.

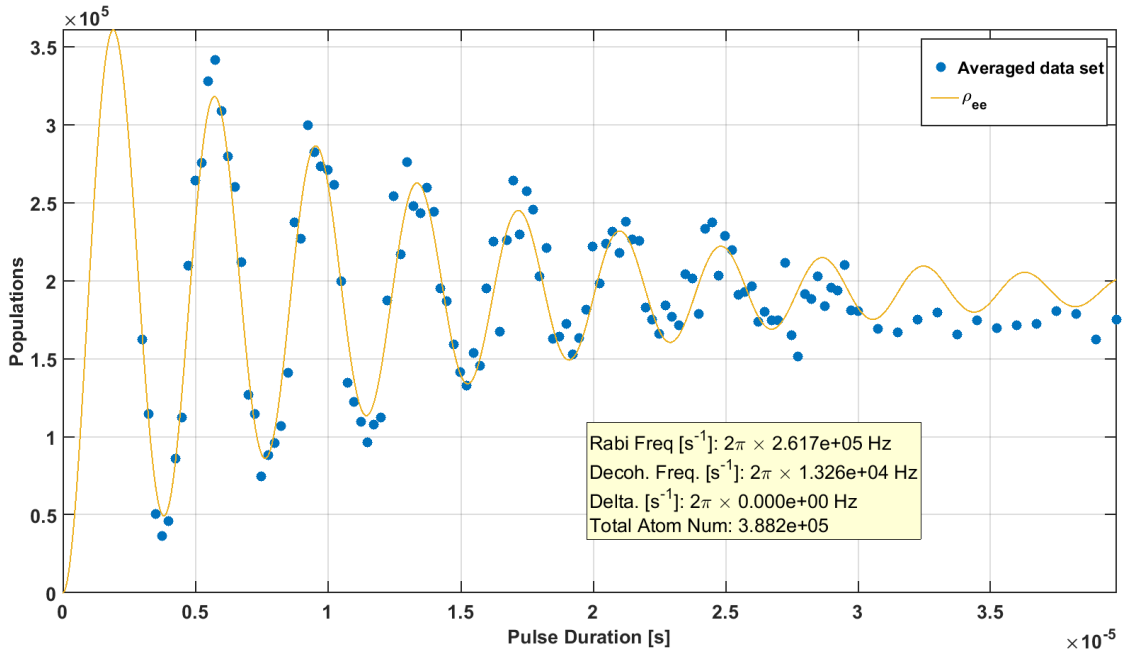

Figure 4.5: Sample data demonstrating Rabi oscillations in a thermal gas, varying the 689 pulse duration on resonance. The population of $^3P_1$ atoms is detected by exciting the atoms, clearing away any that remain in the ground state, waiting for the excited atoms to decay to the ground state, then imaging them. Note the damping of the excited state population as decoherences take over and the populations approaches its equilibrium value.

4.6 Experimental Design Calculations

The eventual goal of the apparatus constructed for this thesis is to optically pump a sample of ^{87}Sr into specific m_F states, then reliably confirm that that this has been achieved. Ideally, the polarization and detection could be performed with light sent through a single optical fiber, and calculations guiding the choices of experimental parameters to achieve this are detailed in the following.

There are a few primary constraints that informed the choices made, with those

arising from detecting the spin population being the more challenging. To begin, the Rabi frequency of the atoms under illumination by the polarizing beam needs to be fast compared to the $1/(2\pi \cdot 7.5 \times 10^3 s^{-1}) = 21\mu$s lifetime of the $^3P_1$ state. Data studying Rabi oscillations induced in ^{86}Sr and observed with the aid of the blow-away beam gave approximate bounds on the Rabi frequencies that the current apparatus and analysis code could detect and fit. The lower bound was estimated to be approximately $\Omega_R/(2\pi)$= 50kHz.

The saturation parameter $s_0 = I/I_{sat}$ is a convenient way to describe many important laser properties. The peak intensity for a Gaussian beam is

$$I = \frac{2P}{\pi r^2} \tag{4.9}$$

where P is the total power in the beam, and r is the $1/e^2$ radius of the beam. With this notation, the Rabi frequency can be expressed as

$$\Omega_R = \Gamma\sqrt{\frac{s_0}{2}} \tag{4.10}$$

The other constraint is that the transitions between different magnetic sublevels must be spectroscopically resolvable when the detection schemes are implemented. This is both a function of the transition's width in frequency space, and the amount by which they are separated from each other. The width of a transition can be broadened beyond that of its natural linewidth γ by many factors, where here power broadening is the concern. A power broadened Lorentzian lineshape has a full width at half maximum of

$$\Delta\omega_{FWHM} = \Gamma\sqrt{1 + s_0} \tag{4.11}$$

The separation of the states will be achieved via the Zeeman effect and application of a magnetic field; see figure 4.4. The coils producing the magnetic field are limited

experimentally to being driven by approximately five amps. With a conversion of about one Gauss per amp of current this means Zeeman shifts up to approximately $\pm$4MHz should be possible for the maximal $\pm m_F$ states.

Given the $\gamma = 7.5$kHz linewidth of the transition, for a beam with a 0.5cm $1/e^2$ radius with a Gaussian profile and 5μW of power, the above equations predict $s_0 = 4.24$ and a power-broadened linewidth of $\Delta f_{FWHM} = 17.2$kHz. For 1mW of power, $s_0 = 850$ and $\Omega_R/(2\pi) = 155$kHz. These parameters are experimentally reasonable, with the power broadening being small enough to allow for the resolution of individual lines in the presence of a moderate (up to 5A) external magnetic field. The 155kHz Rabi frequency similarly satisfies the criteria of being orders-of-magnitude larger than the natural linewidth of the transition.

The beam radius at the location of the atoms was chosen to be 0.5cm, and the necessary optics installed to achieve that size. The size was verified via a Gaussian fitting program analyzing images of the beam from a CCD camera. This beam size is fixed for both the polarization and spectroscopy beams, with only the power varying between the two. Studying the actual Rabi frequencies achieved will provide confirmation of how close these calculations came to reality. The table below summarizes these parameters.

	Pumping	Spectroscopy
Power in Beam	5μW	1mW
s_0	4.25	850
$\frac{\Omega}{2\pi}$	10.9kHz	155kHz
Δf_{FWHM}	17.2kHz	219kHz

Table 4.1: Calculated experimental parameters for the chosen experimental hardware configuration.

For σ_+ polarization, as shown in figure 4.3, $\Delta m_F = +1$ are driven. Natural decay can occur through $\Delta m_F = \{\pm 1, 0\}$ transitions, but in general the effect of applying σ_+ light is to drive the atoms towards the $m_F = +9/2$ ground state. They remain in this ground state, as it is dark to the polarizing photons for reasons discussed in section 4.3. Reversing the light polarization would ultimately drive atoms towards the opposite ($m_F = -9/2$) stretched state.

Chapter 5

Experimental Particulars

5.1 Hardware Overview

The bulk of the hardware designed and constructed for this thesis is used to apply the appropriate 689nm laser light to the atoms for implementing spin polarization via optical pumping. As mentioned earlier, the new apparatus also lays the groundwork for implementing the optical Stern-Gerlach (OSG) technique. While OSG is not the focus of this thesis, the hardware related to it is discussed here as the technique will be a useful tool employed in the near future for spin-state detection.

Given the crowded environment around the experimental vacuum chamber, there were numerous space constraints when choosing how to appropriately shape, route, and control the laser light that ultimately illuminates the atomic sample at the center of the chamber. Both optical-table space, and constraints due to the location of other hardware (e.g. LN_2 trap, trim coils, lattice breadboard) limit access to the various transparent viewports that allow light to reach the atoms. The spin polarization and OSG light were chosen to enter the chamber vertically downward, parallel to one axis ("arm C") of the existing 532nm optical lattice. This provides flexibility in the equipment that can be attached, though also necessitates the construction of a

substantial amount of hardware such as pillars, brackets, and connectors, as described in this chapter.

A basic overview of the hardware is as follows. Laser light for the various beams is sent via fiber optic to output collimators housed in an optical cage system. The cage system incorporates the necessary beam cubes, lenses, and turning mirrors to combine the beams, shape them, and route them onto the atoms. The cage system is mounted above the main experimental chamber by a series of custom-machined parts, and these parts hold additional optical components. The parts necessary to implement a 461nm blow-away beam, allowing the removal of ground state atoms from the traps, were also constructed and installed.

5.1.1 Lattice Beam Propagation

The optical lattice is formed by retroreflecting a 532nm beam. The new hardware also retroreflects the beam of the lattice, while incorporating the downward propagating 689nm spin polarization and OSG beams. To accomplish this, a flat dichroic mirror (CVI Optics Y2-1025-0) was used, which is coated to reflect high power 532nm light and pass 689nm. The CVI Y2 optic has 90% transmission of 689nm light. Because the dichroic is flat, the retroreflected lattice beam needs to be focused back down to match the first pass size. This is accomplished with a 300mm focal langth lens coated for 532nm light (CVI Optics PLCX-25.4-149.9-UV-532). Placed 14.6cm from the atoms, this lens is as low as possible without interfering with the MOT optics, which are pulled back pneumatically when the high-power lattice light is sent through the chamber. Accounting for the distance between the dichroic and lens, the total single pass geometric distance from the atoms to the dichroic is 17.5cm. The spot sizes at the location of the atoms was predicted by a *Matlab* Gaussian beam propagation program, the results of which are shown in table 5.1 and figure 5.1 below.

	Vertical (um)	Horizontal (um)
First pass	186	207
Retroreflection	250	194

Table 5.1: Predicted lattice beam parameters with the inclusion of the new f=300mm lens and dichroic mirror.

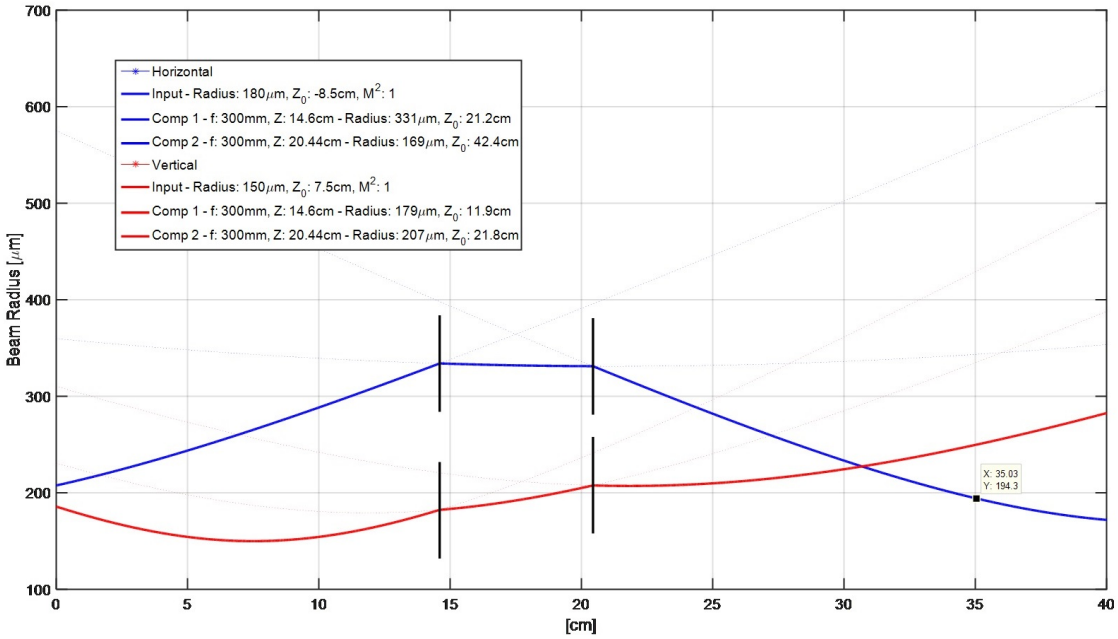

Figure 5.1: Predicted lattice beam behavior (first pass and retroreflection) with new f=300mm lens and dichroic mirror. Atoms are located at 0cm and 35cm (retro) along the horizontal axis.

5.2 Cage System

The primary hardware responsible for shaping and directing the OSG and spin polarization beams is the new optical cage system. The cage system is constructed primarily out of Thorlabs 30mm cage system components and custom-machined parts. These parts are mounted to a 0.5" thick, double-density optical breadboard (1/4-

20 tapped Newport Corporation SA2-12X18-D). The OSG and polarization beams propagate horizontally in two separate planes ("layers"), with the OSG layer on top. These are then reflected vertically downward through various other optical elements, towards the atoms in the vacuum chamber. To allow flexibility in future additions to the system, the apparatus was designed to be modular, and additional optical breadboard space is available.

Both the OSG and spin polarization portions of the cage system follow the same basic form, including fiber output collimators in kinematic mounts, a combining polarizing beam splitter (PBS), kinematic right-angle mirror mount, and pick-off to a monitor photodiode. See figure 5.2 below for a picture of the cage system, without the additional mounting hardware, and figure 5.5 for a closeup of the mounted cage and optical elements. Both the OSG and polarization layers contain two kinematic fiber launchers which send their two beams into a beam cube. With the appropriate linear polarization, the beams reflect or pass though the PBS and can combined and made to co-propagate though the system.

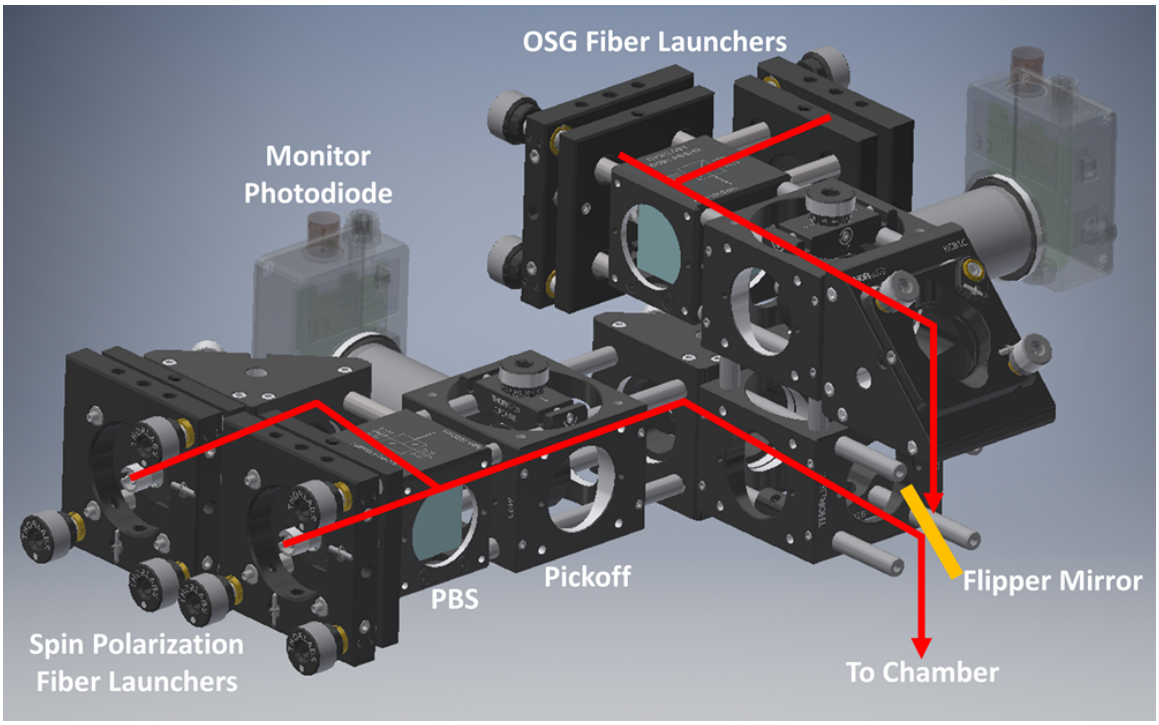

Figure 5.2: Cage system for routing both optical Stern-Gerlach (upper level) and spin polarization (lower level) light into the main experimental chamber. Red lines indicate the beam paths. The Thorlabs C6W cage cubes enclose wedge beam samplers held in CP360R mounts to pick off light and send it to an attached monitoring photodiode. The position of a motorized flipper selects whether the OSG or spin polarization light is routed to the chamber.

A motorized flipper (Thorlabs MFF101) holds a 45°-angled 1" mirror at the point where the OSG and polarization beams would intersect. Using TTL-logic, the inclusion or exclusion of this mirror into the path selects which beams (either OSG *or* polarization) are directed down into the chamber. Vibrations and stray magnetic fields are a concern. Mounting the flipper near the vacuum chamber and actuating it produced no effects on the nearby trapped atoms or laser systems. The time for the mirror to flip out of the way was measured using a HeNe laser and photodiode. With the beam centered on the mirror, the photodiode signal took about 3ms to rise

or drop between 90% and 10% of it's value.

While this time is sufficiently fast for the current needs, there is a 300ms delay between the TTL signal, and the phoptodiode's response, which will have to be accounted for in the experimental cycle. The flipper-motor, when actuated, is positioned at the appropriate height to catch the spin-polarization beam and send it downward through the center of the vacuum chamber. When actuated, the mirror flips out of the way of the downward propagating OSG beams, and allows them to pass to the chamber while the polarization beam is no longer reflected. See the following figure for a schematic of this hardware.

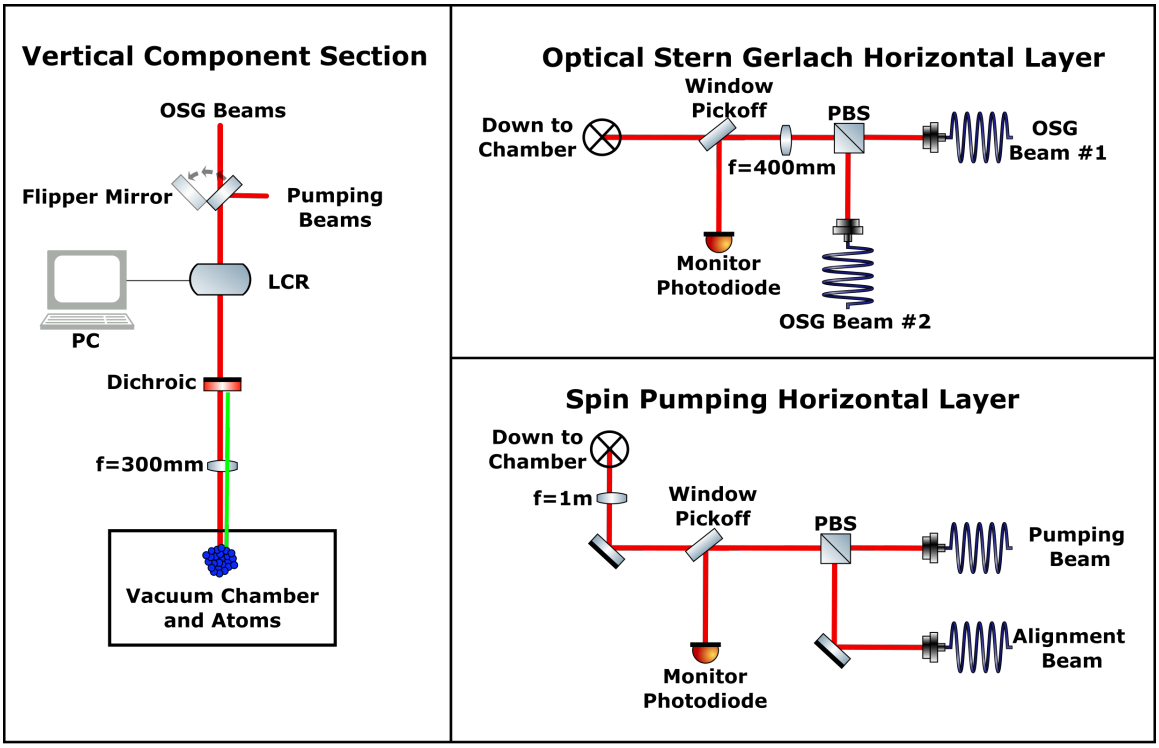

Figure 5.3: Optics for routing both optical Stern-Gerlach (upper level) and spin polarization (lower level) light into the main experimental chamber, as well as shaping the beam and controlling its polarization.

5.2.1 Polarization Layer

For the spin polarization layer, the beam passing through the PBS (versus the port that reflects light) is used for both spin polarization, and shelving spectroscopy. This beam's frequency is tuned to that of the ${}^1S_0\,|F = 9/2, m_F\rangle \rightarrow {}^3P_1\,|F = 9/2, m_F\rangle$ transition on which the stir beam operates (see figure 3.2). The zeroth order of the stir beam AOM is picked off, sent through another AOM to allow for polarization beam frequency control, and coupled into the optical fiber leading to the cage system. As described in chapter four section six, this beam was designed to have a $1/e^2$ radius of 0.5cm at the atoms. A 1m focal length lens 25.3cm from the Thorlabs TC12APC-633 fiber launcher achieves this, as measured by a CCD camera and beam profiling software. This beam was designed to operate at 5μW of power for the spin polarization, and 1mW for the shelving spectroscopy. The second fiber coupler in the polarization layer is used to send an alignment beam for the optical lattice along the same path without having to disturb the fiber used for polarization.

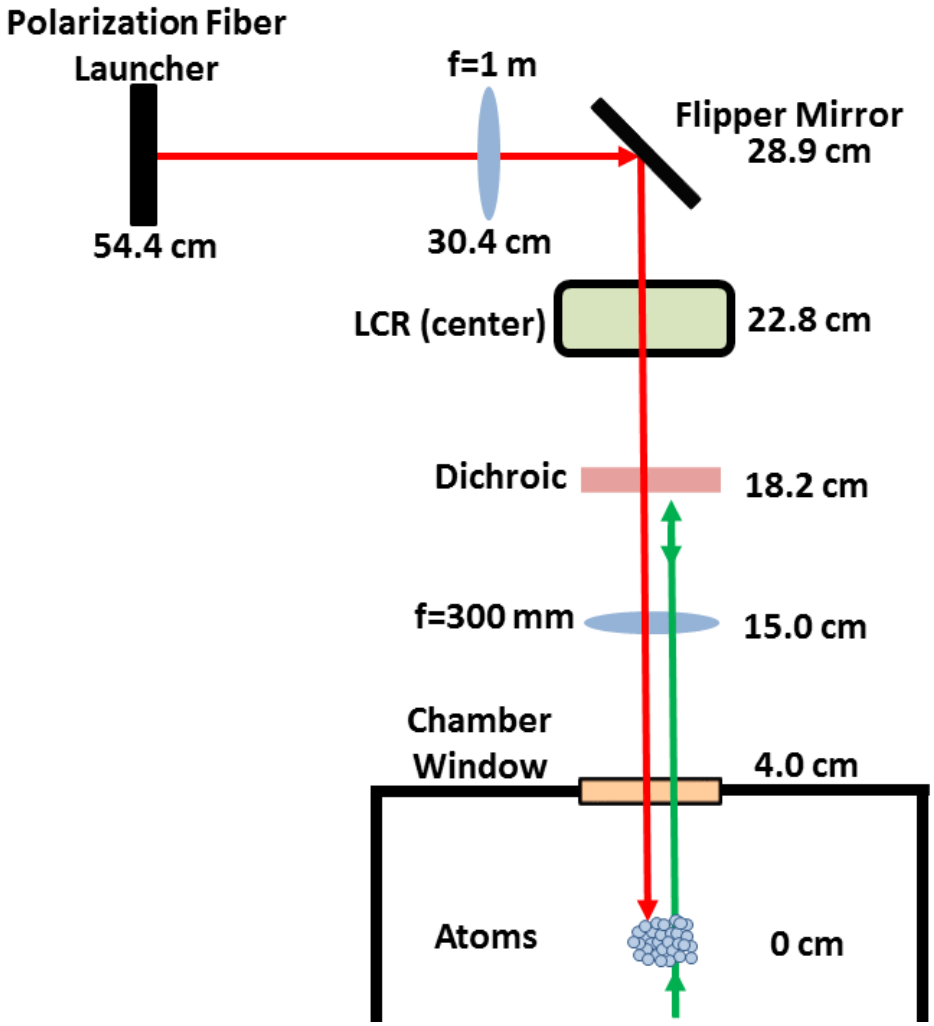

Figure 5.4: Schematic of the polarization laser distances to various components (referenced to atom position). Note that these include the additional {3.6mm, 2.8mm, 13mm} optical path length increase due the index of refraction of the {chamber window, dichroic, LCR}.

5.2.2 OSG Layer

The OSG layer also contains two fiber launchers, which will be used to overlap the separate beams needed for this technique [31]. Compared to spin polarization, the OSG beams require tighter tolerances, and small waists of about 60μm. These toler-

ances make knowledge of the *optical* path lengths to various components crucial, so they are documented in the appendix. I emphasize the word optical to point out that these distances include the changes in the path length due to variations in the index of refraction. A 400mm focal length lens 11.6cm from the Thorlabs TC12APC-633 fiber launcher is predicted to produce the desired waist size at the atoms.

5.2.3 LCR

In addition to their shape and location, the polarization state of the beams passing through to the chamber needs to be accurately switched between left circular, right circular, and linear. Incorporating this polarization change into the *Labview* control software routine is desirable, so a computer-controlled variable waveplate is needed. This is accomplished by a liquid crystal retarder (LCR) in the path. A MeadowLark Optics LV-300 LCR controlled by a driver produced by the same manufacturer is used. The driver sends a variable amplitude 20kHz square wave to the device, the amplitude of which determines the retardance, and thus polarization state, of the light passing though it. The LCR is secured to an custom-machined L-shaped bracket directly above the gimbal-mounted dichroic mirror. The L-bracket is aligned at 45° so that the adjustment axes of the dichroic mirror are aligned with arms A and B of the optical lattice. See the following picture of the LCR mounted in-place, along with other hardware.

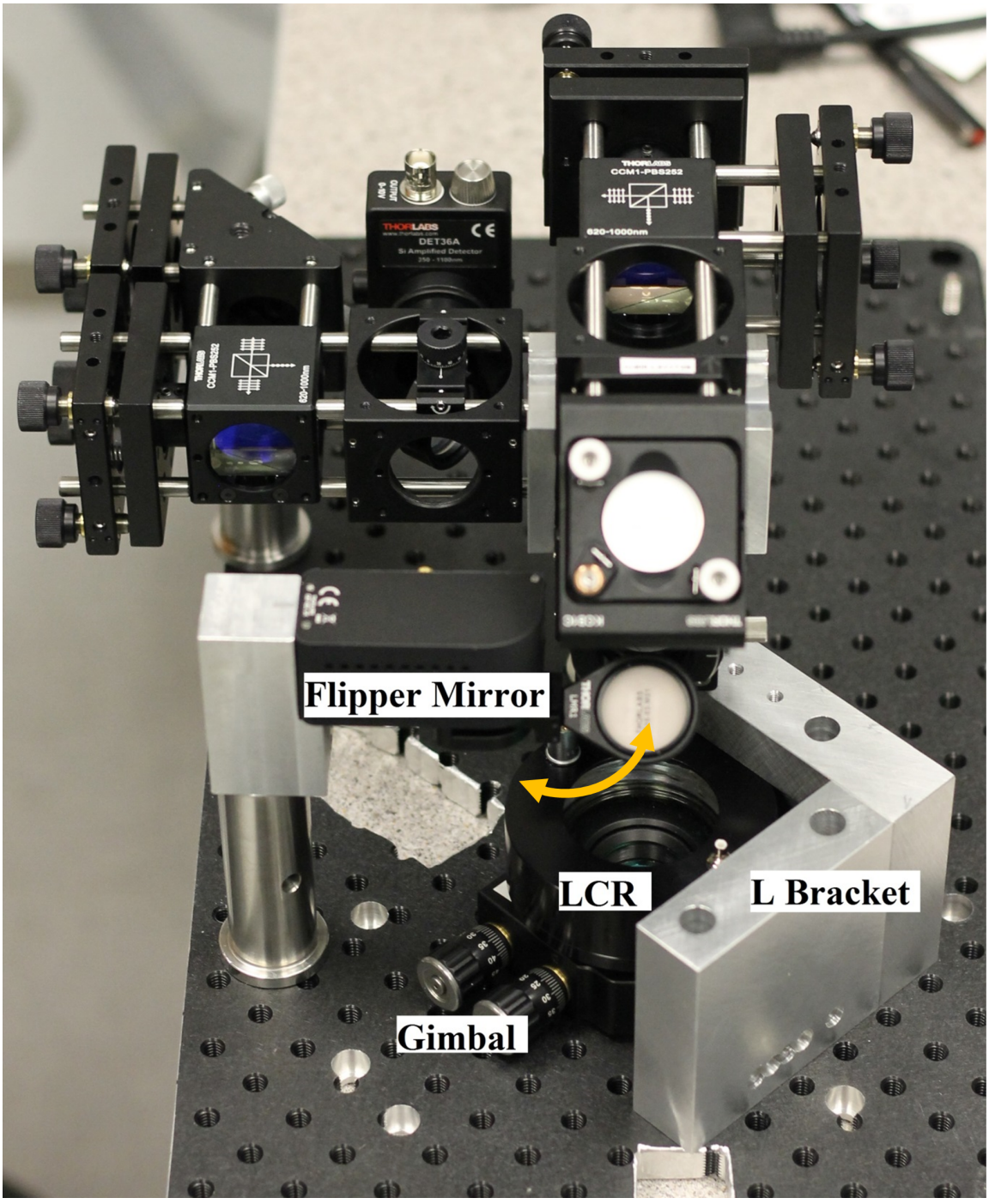

Figure 5.5: Picture of the breadboard, flipper motor, cage system, and breadboard.

Two brief technical warnings are in order when using the LCR:

- The device can be ruined by even a brief application of DC voltage (instead of

20kHz-square)to it's input.

- The 8-32 mounting screw can only penetrate about 0.2in into the housing before running into the optical material (no manufactured stop to prevent this).

5.2.4 Mounting Hardware and L-Bracket

It was nontrivial to attach the aforementioned cage system and optical breadboard to the preexisting vacuum chamber, given the space constraints. A number of aluminum parts were designed and machined to accomplish this. The cage system and breadboard stand above the main vacuum chamber on three rectangular pillars which screw down into the 1/4-20 threaded bolt circle on the chamber-top flange. Two of these pillars are shorter than the third, with the difference being made up by a horizontal "lens bar" between them. The lens bar contains tapped mounting holes for the breadboard, as well as a recess for the detachable lens mount. The lens mount is SM-1 threaded to hold the f= 300mm lattice retro lens via locking rings. It is also angled at 5° to divert any reflections away from the atoms, and the region of the optical lattice. The breadboard attaches to the chamber pillars via counterbored 1/4-20 holes. The cage system and flipper motor attach to the breadboard from underneath by 1/4-20 holes tapped into the bottom of 1" diameter pillars. See figures 5.6 and 5.7 below for CAD drawings of the parts in-situ.

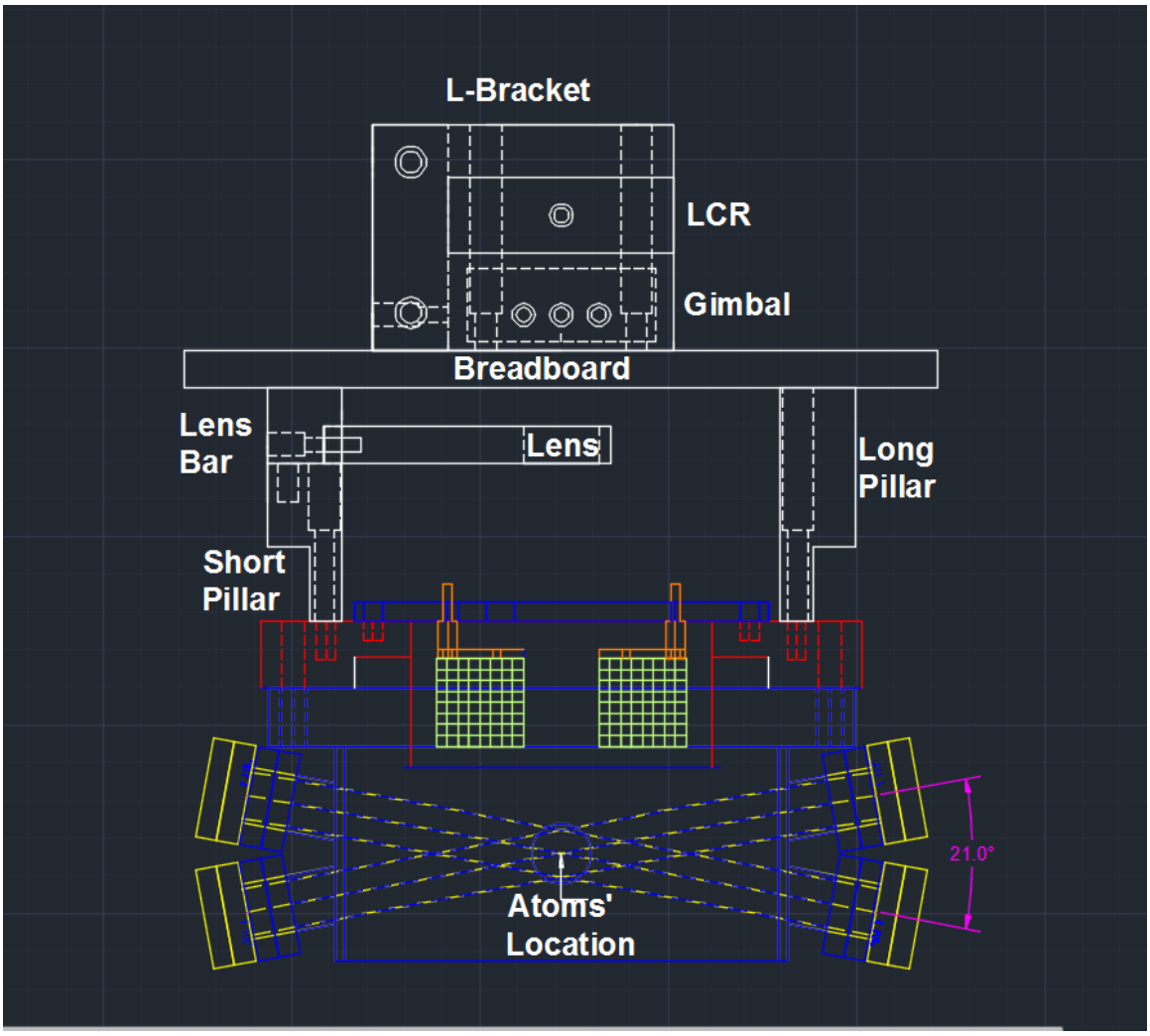

Figure 5.6: Side view of the main experimental vacuum chamber, showing the hardware designed to support the spin manipulation cage system, as well as to hold the lattice arm C retro lens and dichroic.

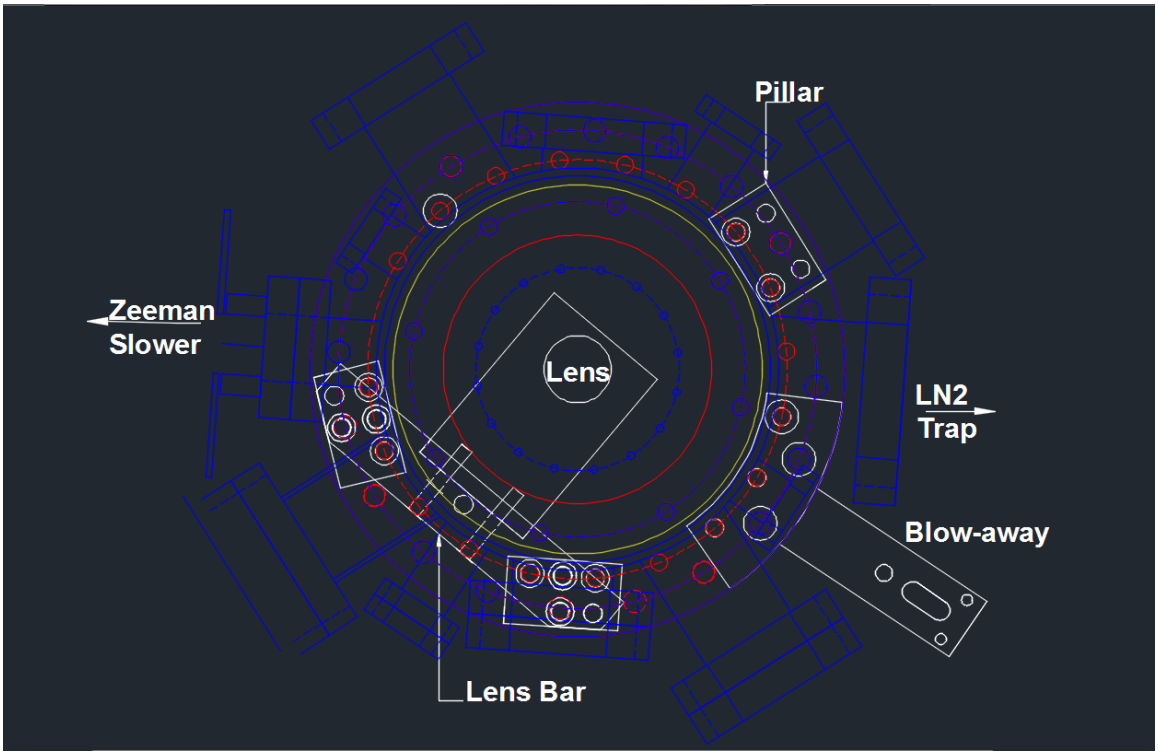

Figure 5.7: Top-down view of the vacuum chamber, showing the hardware to center the arm C lattice retro lens (detachable) on the atoms at an appropriate height. The mount connecting the 461nm blow-away beam to the chamber is also shown.

To hold the LCR and gimbal-mounted-dichroic at the appropriate heights and centered on the atoms, an L-shaped bracket was made. This bracket is comprised of two aluminum blocks screwed together and attached to the top of the optical breadboard. The LCR is mounted in a recessed slot via its single 8-32 tapped hole, and the gimbal is held below the LCR. The figure below depicts this assembly from a top-down view.

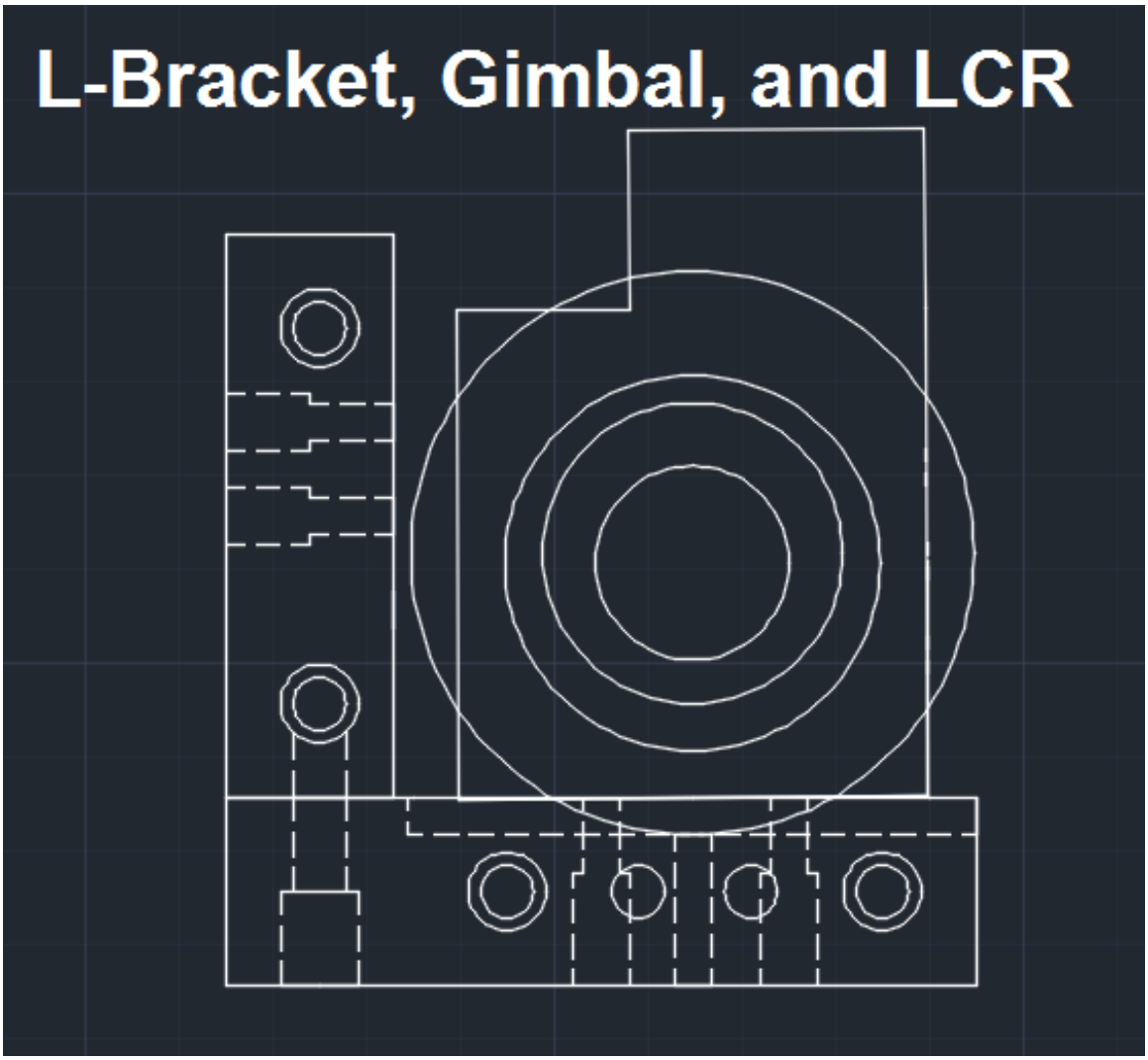

Figure 5.8: Top-down (towards chamber) view of the L-bracket designed to support the arm-C lattice retro dichroic in its Thorlabs GM100 gimbal, as well as the MeadowLark Optics LV-300 liquid crystal retarder (LCR). This bracket attaches to the top of the optical breadboard, above the vacuum chamber.

See the appendix at the end of this document for optical path lengths from the atoms to various components.

5.3 461nm Blow-Away Beam

The ability to selectively remove ground-state atoms from the experiment is a useful tool for both trap diagnostics, and experimental procedures. The parts to allow for such a "blow-away" or "clearing" beam on the apparatus were constructed and implemented. This beam scatters enough 461nm photons from the ground state atoms to knock them out of the red MOT or ODT.

The light for this beam is derived from that of the imaging beam, which is used to take the absorption images that comprise the majority of the data. Zeroth order light from the vertically-mounted "image AOM #1 " (second AOM of the imaging chain) was separated off by a horizontally-oriented D-mirror after passing through a +300mm focal length shaping lens 88.5cm from the AOM. After being allowed to propagate for a sufficient distance to mode-match into an optical fiber for maximum coupling efficiency, the beam passes through another AOM who's first order light enters a fiber collimator 106.1cm from the lens. The mechanical drawing for the custom attachment made to connect this AOM to a Thorlabs PY005 five-axis kinematic mount is provided in the appendix, and a beam path schematic is depicted below.

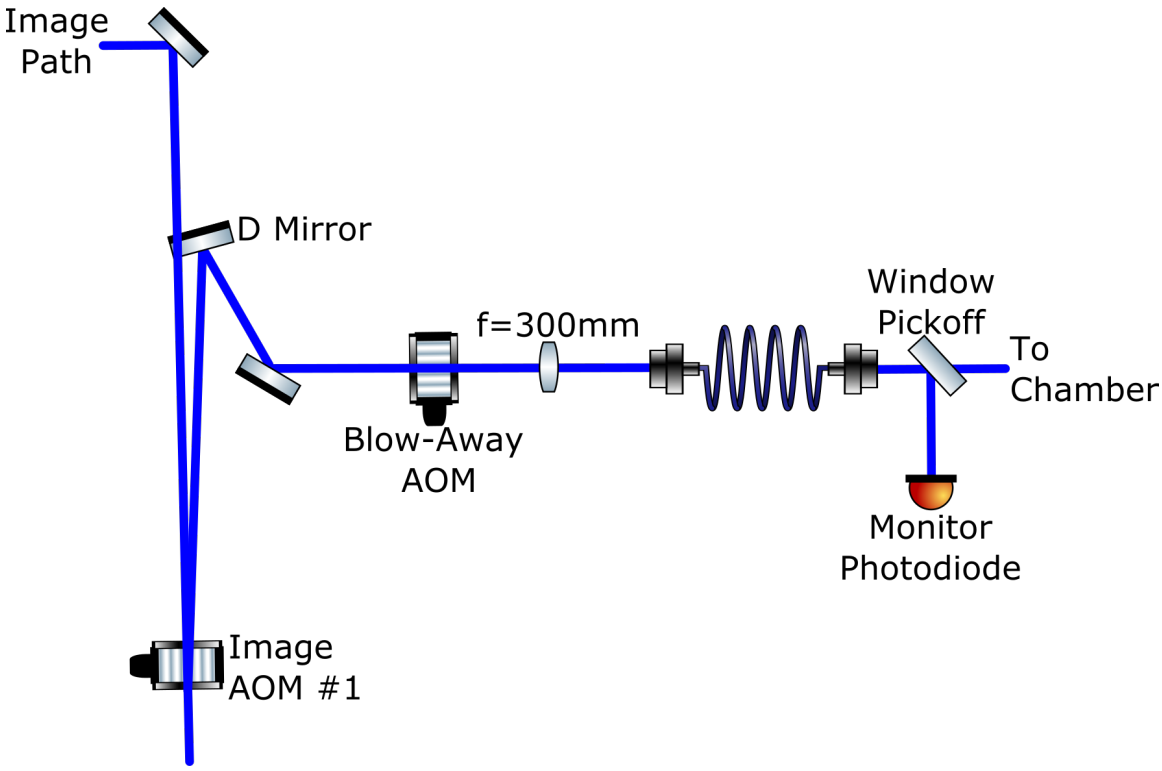

Figure 5.9: Blow-away beam optical schematic.

Sending the negative first order light of this final AOM (IntraAction Corp. ATM-802DA1, 80MHz center frequency, 151ns/nm rise time), allows shifting the laser's frequency back onto resonance, and the ability to quickly turn the beam on or off. The latter is particularly important, as atoms are excited to the 21us lifetime $^3P_1$ state. The blow-away pulse must clear out the ground state atoms before an appreciable amount of excited state atoms have time to decay back down. Atoms found in the ground state after the clearing pulse give a count of those that were in the $^3P_1$ state when the pulse was being applied, since the excited state atoms cannot be imaged directly.

To quantify the population of atoms excited to the $^3P_1$ state a 689nm excitation pulse is applied to the atoms, any that remain in the ground state are cleared away with the blow-away 461nm beam, the excited atoms then decay to the ground state

where they are directly imaged (counted).

After coupling 12.5mW/23mW≈ 54% through a five-meter optical fiber (Thorlabs P3-488PM-FC-5), the beam exits a fixed collimator (Thorlabs F240APC-532) and is sent though a window pickoff to a power-monitoring photodiode and also through a viewport in the vacuum chamber. The output collimator, it's kinematic mount (Thorlabs KAD12F) are attached to a small section of 30mm cage system. The crowded area around the chamber viewports necessitated the machining of a custom mount to attach the apparatus to a 1/4-20 bolt-circle on the bottom of the vacuum chamber (see appendix and figure 5.10).

The CAD snapshot below depicts the how the chamber mount supports the fiber launcher and pickoff window. Using the blow-away beam to clear out ground state atoms, Rabi oscillations are directly observable (see figure 4.5).

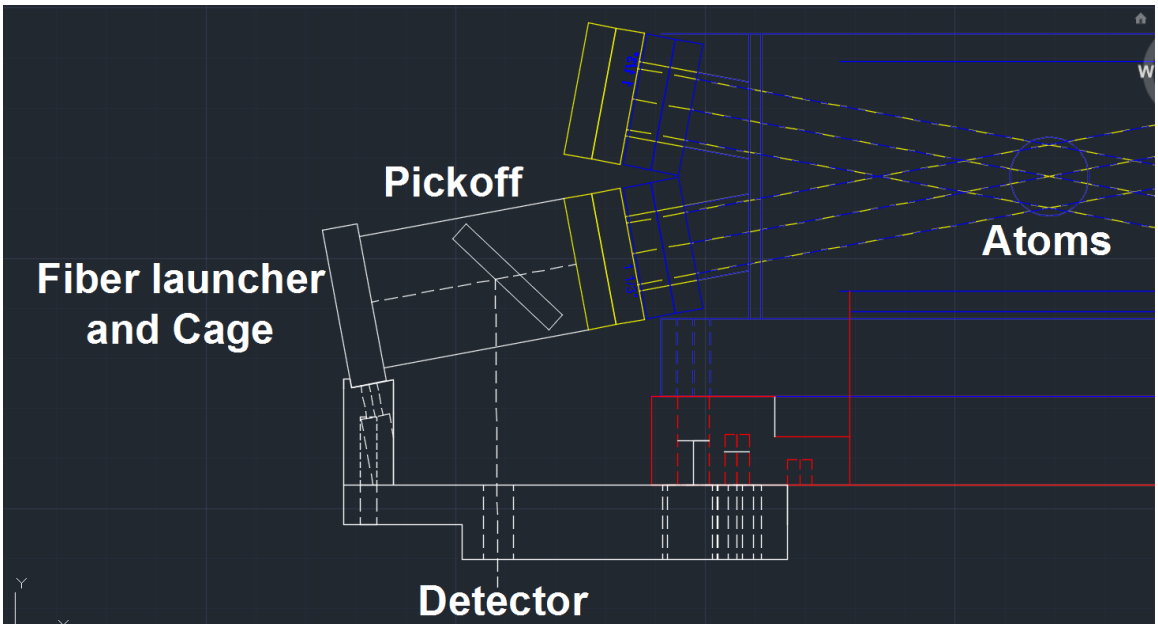

Figure 5.10: Side view of the hardware, mounted to the vacuum chamber at the appropriate angle to send fiber-coupled 461nm light though a mini-viewpoint in the chamber to blow away ground state atoms.

Chapter 6

Conclusion

6.1 Conclusion and Future Direction

To conclude, this thesis details the design and construction of the hardware necessary to implement a number of spin manipulation techniques in ultracold gasses of ^{87}Sr. The apparatus operates using light scattering on the $^1S_0\,|F = 9/2, m_F\rangle \rightarrow {}^3P_1\,|F = 9/2, m'_F\rangle$ transition in strontium, at 689nm. The hardware is comprised of an optical cage system mounted atop a various custom-machined supports and brackets. In addition, a blow-away beam apparatus was designed, constructed, and implemented to clear away ground state atoms.

The hardware described here will be used in the near future to both spin polarize samples of ^{87}Sr, and quantify the resulting spin-state imbalance. More generally, it will be used to alter the populations of atoms in the ground-state magnetic (m_F) sublevels of the $|F = 9/2, m_F\rangle$ state via optical pumping. Furthermore, this hardware lays the foundation for more advanced spin manipulation techniques such as optical Stern-Gerlach technique. Such techniques will be valuable state-preparation and diagnostic tools for upcoming experiments studying quantum magnetism in systems with many spin-components.

References

[1] Nobel Prize in Physics 1966 - Presentation Speech.

[2] Tomoya Akatsuka, Masao Takamoto, and Hidetoshi Katori. Optical lattice clocks with non-interacting bosons and fermions. *Nature Physics*, 4(12):954–959, December 2008.

[3] J. F. Barry, D. J. McCarron, E. B. Norrgard, M. H. Steinecker, and D. DeMille. Magneto-optical trapping of a diatomic molecule. *Nature*, 512(7514):286–289, August 2014.

[4] Immanuel Bloch, Jean Dalibard, and Sylvain Nascimbne. Quantum simulations with ultracold quantum gases. *Nature Physics*, 8(4):267–276, April 2012.

[5] B. J. Bloom, T. L. Nicholson, J. R. Williams, S. L. Campbell, M. Bishof, X. Zhang, W. Zhang, S. L. Bromley, and J. Ye. An optical lattice clock with accuracy and stability at the 10-18 level. *Nature*, 506(7486):71–75, February 2014.

[6] P. Bouyer, P. Lemonde, M. Ben Dahan, A. Michaud, C. Salomon, and J. Dalibard. An Atom Trap Relying on Optical Pumping. *EPL (Europhysics Letters)*, 27(8):569, 1994.

[7] Martin M. Boyd. *High Precision Spectroscopy of Strontium in an Optical Lattice: Towards a New Standard for Frequency and Time*. PhD Thesis, University of Colorado, Boulder, Colorado, USA.

[8] G. Cappellini, M. Mancini, G. Pagano, P. Lombardi, L. Livi, M. Siciliani de Cumis, P. Cancio, M. Pizzocaro, D. Calonico, F. Levi, C. Sias, J. Catani, M. Inguscio, and L. Fallani. Direct Observation of Coherent Interorbital Spin-Exchange Dynamics. *Physical Review Letters*, 113(12):120402, September 2014.

[9] Miguel A. Cazalilla and Ana Maria Rey. Ultracold Fermi gases with emergent SU(N) symmetry. *Reports on Progress in Physics*, 77(12):124401, 2014.

[10] I. Courtillot, A. Quessada-Vial, A. Brusch, D. Kolker, G. D. Rovera, and P. Lemonde. Accurate spectroscopy of Sr atoms. *The European Physical Journal D*, 33(2):161–171, May 2005.

[11] Y. N. Martinez de Escobar, P. G. Mickelson, M. Yan, B. J. DeSalvo, S. B. Nagel, and T. C. Killian. Bose-Einstein Condensation of 84sr. *Physical Review Letters*, 103(20):200402, November 2009.

[12] B. J. DeSalvo. *Ultralong-Range Molecules and Rydberg Blockade in Ultracold 86Sr*. PhD. Thesis, Rice University, Houston, Texas, USA, 2015.

[13] B. J. DeSalvo, M. Yan, P. G. Mickelson, Y. N. Martinez de Escobar, and T. C. Killian. Degenerate Fermi Gas of $ˆ{87}\mathrm{Sr}$. *Physical Review Letters*, 105(3):030402, July 2010.

[14] Richard P. Feynman. Simulating physics with computers. *International journal of theoretical physics*, 21(6):467–488, 1982.

[15] Christopher Foot. *Atomic Physics*. Oxford University Press, 2008.

[16] Takeshi Fukuhara, Seiji Sugawa, Yosuke Takasu, and Yoshiro Takahashi. All-optical formation of quantum degenerate mixtures. *Physical Review A*, 79(2):021601, February 2009.

[17] Walther Gerlach and Otto Stern. Der experimentelle Nachweis der Richtungsquantelung im Magnetfeld. *Zeitschrift fr Physik*, 9(1):349–352, December 1922.

[18] A. V. Gorshkov, M. Hermele, V. Gurarie, C. Xu, P. S. Julienne, J. Ye, P. Zoller, E. Demler, M. D. Lukin, and A. M. Rey. Two-orbital SU(N) magnetism with ultracold alkaline-earth atoms. *Nat Phys*, 6(4):289–295, April 2010.

[19] Rudolf Grimm, Matthias Weidemller, and Yurii B. Ovchinnikov. Optical Dipole Traps for Neutral Atoms. *Advances In Atomic, Molecular, and Optical Physics*, 42:95–170, January 2000.

[20] Christian Hofrichter, Luis Riegger, Francesco Scazza, Moritz Hfer, Diogo Rio Fernandes, Immanuel Bloch, and Simon Flling. Direct Probing of the Mott Crossover in the SU(N) Fermi-Hubbard Model. *Physical Review X*, 6(2):021030, June 2016.

[21] L. Isaev, J. Schachenmayer, and A. M. Rey. Spin-Orbit-Coupled Correlated Metal Phase in Kondo Lattices: An Implementation with Alkaline-Earth Atoms. *Physical Review Letters*, 117(13):135302, September 2016.

[22] D. Jaksch and P. Zoller. The cold atom Hubbard toolbox. *Annals of Physics*, 315(1):52–79, January 2005.

[23] T. C. Killian, S. Stellmer, and F. Schreck. Degenerate Quantum Gases of Strontium. In K. Madison, K. Bongs, L. Carr, A. M. Rey, and H. Zhai, editors, *Annual Review of Cold Atoms and Molecules*, volume 2. World Scientific Publishing Company, May 2014.

[24] Thomas H. Loftus, Tetsuya Ido, Martin M. Boyd, Andrew D. Ludlow, and Jun Ye. Narrow line cooling and momentum-space crystals. *Physical Review A*, 70(6):063413, December 2004.

[25] P. G. Mickelson. *Trapping and Evaporation of 87Sr and 88Sr Mixtures*. PhD Thesis, Rice University, Houston, Texas, USA, 2010.

[26] Takashi Mukaiyama, Hidetoshi Katori, Tetsuya Ido, Ying Li, and Makoto Kuwata-Gonokami. Recoil-Limited Laser Cooling of $ˆ{87}\mathrm{S}\mathrm{r}$ Atoms near the Fermi Temperature. *Physical Review Letters*, 90(11):113002, March 2003.

[27] Travis Nicholson. *A new record in atomic clock performance*. PhD thesis, University of Colorado, CO, USA, 2015.

[28] Guido Pagano, Marco Mancini, Giacomo Cappellini, Pietro Lombardi, Florian Schfer, Hui Hu, Xia-Ji Liu, Jacopo Catani, Carlo Sias, Massimo Inguscio, and Leonardo Fallani. A one-dimensional liquid of fermions with tunable spin. *Nature Physics*, 10(3):198–201, March 2014.

[29] William D. Phillips. Nobel Lecture: Laser cooling and trapping of neutral atoms. *Reviews of Modern Physics*, 70(3):721, 1998.

[30] F. Scazza, C. Hofrichter, M. Hfer, P. C. De Groot, I. Bloch, and S. Flling. Observation of two-orbital spin-exchange interactions with ultracold SU(N)-symmetric fermions. *Nature Physics*, 10(10):779–784, October 2014.

[31] Simon Stellmer, Rudolf Grimm, and Florian Schreck. Detection and manipulation of nuclear spin states in fermionic strontium. *Physical Review A*, 84(4):043611, October 2011.

[32] Simon Stellmer, Meng Khoon Tey, Bo Huang, Rudolf Grimm, and Florian Schreck. Bose-Einstein Condensation of Strontium. *Physical Review Letters*, 103(20):200401, November 2009.

[33] Masao Takamoto. Improved Frequency Measurement of a One-Dimensional Optical Lattice Clock with a Spin-Polarized Fermionic 87sr Isotope. *Journal of the Physical Society of Japan*, 75(10):104302, October 2006.

[34] Meng Khoon Tey, Simon Stellmer, Rudolf Grimm, and Florian Schreck. Double-degenerate Bose-Fermi mixture of strontium. *Physical Review A*, 82(1):011608, July 2010.

[35] H. G. C. Werij, Chris H. Greene, C. E. Theodosiou, and Alan Gallagher. Oscillator strengths and radiative branching ratios in atomic Sr. *Physical Review A*, 46(3):1248–1260, August 1992.

Appendix A

Appendices

A.1: **Calculation of Hyperfine Parameters and g-factors**

A.2: **Optical Distances for OSG and Polarization Hardware**

A.3: **Blow-Away Machine Parts Drawings**

A.4: **Optical Pumping and OSG Machine Parts Drawings**

Table A.1: Appendix Contents

A.1 Calculation of Hyperfine Parameters and g-factors

I calculate the Landè g-factor for the total angular momentum (g_F), and then the relevant hyperfine-isotope energy shifts for ^{87}Sr. The nuclear g_I factor of ^{87}Sr is

$$g_I = \frac{\mu_I(1-\sigma_d)}{|I|\mu_B} = -0.0001318 \tag{A.1}$$

where $\sigma_d = 0.00345$ is the diamagnetic correction factor, and $\mu_I = -1.0924\mu_N$ is the nuclear magnetic moment expressed as a multiple of the nuclear magneton [7]. Taking the electron's orbital g-factor $g_L = 1$, and $g_e \approx 2$, the total g-factor of the

electron and atom are state-dependent, and defined as follows

$$g_J = g_S \frac{J(J+1) - L(L+1) + S(S+1)}{2J(J+1)} + g_L \frac{J(J+1) + L(L+1) - S(S+1)}{2J(J+1)} \quad \text{(A.2)}$$

$$g_F = g_J \frac{F(F+1) - I(I+1) + J(J+1)}{2F(F+1)} + g_I \frac{F(F+1) + I(I+1) - J(J+1)}{2F(F+1)} \quad \text{(A.3)}$$

Furthermore, the energy shifts (in Hz) from an $I = 0$, state are given by

$$\Delta E_{HFS}/h = \frac{A}{2}K + \frac{Q}{2}\frac{\frac{3}{4}K(K+1) - I(I+1)J(J+1)}{I(2I-1)J(2J-1)} \quad \text{(A.4)}$$

where A and Q are the magnetic dipole and electric quadruple interaction constants respectively, and

$$K = F(F+1) - I(I+1) - J(J+1) \quad \text{(A.5)}$$

I have calculated the g_F and energy between hyperfine states (ΔE_{HFS}) for ^{87}Sr transitions of interest in the following table using information from M. Boyd's thesis[7]. Note that in his thesis, Boyd neglects the contribution of g_I to g_F as it is orders of magnitude smaller, making g_F exactly zero. I have also done this, which is why the $J = 0$ $^1S_0$ and $^3P_0$ states are listed as having $g_F = 0$; the purely nuclear contribution to the energy is only $\approx 200\text{Hz/G}\cdot m_F$. See the *Mathematica* code in that follows for the calculation details.

State ($^{2S+1}L_J$)	A(MHz)	Q(MHz)	F	g_F	ΔE_{HFS} (MHz)
$^1S_0$	0	0	9/2	0	0.00
$^1P_1$	-3.4	39	7/2	-2/9	36.58
			9/2	4/99	-22.60
			11/2	2/11	-5.55
$^3P_0$	0	0	9/2	0	0.00
$^3P_1$	-260.084	-35.658	7/2	-1/3	1414.12
			9/2	2/33	283.86
			11/2	3/11	-1179.29
$^3P_2$	-212.765	67.34	5/2	-6/7	2317.28
			7/2	-1/7	1597.14
			9/2	2/11	618.65
			11/2	51/143	-551.55
			13/2	6/13	-1898.05

Table A.2: Calculated g-factors and hyperfine-isotope energy shifts for ^{87}Sr, *referenced to an* $I = 0$ *state.*

```
(*See pg. 124 of Martin Boyd's Thesis*)
ClearAll["Global`*"]
(* ---------------------- Calculation of g
 factors ------------------------------------- *)

i  = 9/2;
J = 2;
S = 1;
L = 1;
F = 5/2;

μn = 5.051 * 10^-27; (* Nuclear magneton in Joules/Tesla *)
μB = 9.274 × 10^-24; (* Bohr magneton *)
μi = -1.0924 μn;
σ = 0.00345; (* Diamagnetic correction factor *)
gi = μi (1 - σ) / (μB i); (* nuclear g-factor of 87Sr = -0.0001318*)
(*So the electron gs=2 is ~4 orders of magnitude larger*)
gL = 1; (* Electron orbital g factor *)
gs = 2; (* Electron spin g factor  *)


gj = gL (J (J + 1) - S (S + 1) + L (L + 1)) / (2 J (J + 1)) + gs (J (J + 1) + S (S + 1) - L (L + 1)) / (2 J (J + 1));
gF = gj (F (F + 1) - i (i + 1) + J (J + 1)) / (2 F (F + 1)) + gi (F (F + 1) + i (i + 1) - J (J + 1)) / (2 F (F + 1));

(* ---------------------- Calculation
 of HF Energy Level Shifts ------------------ *)
A = -212.765 * 10^6;
Q = 67.34 * 10^6;
K = F (F + 1) - i (i + 1) - J (J + 1);
ΔEHFS = (A/2 K + Q/2 (3/4 K (K + 1) - i (i + 1) J (J + 1)) / (i (2 i - 1) J (2 J - 1))) * 10^-6
```

```
2371.28
```

Printed by Wolfram Mathematica Student Edition

A.2 Optical Distances for OSG and Polarization Hardware

Component	**Dichroic**	**Chamber Window**	**LCR**
Geometric Thickness (mm)	6.4	8	25.4
Optical Thickness (mm)	9.2	11.6	38.4
Distance Change (mm)	2.8	3.6	13

Table A.3: Optical path length changes through various optical components. Note that the indexes of refraction at 689nm for the chamber window and LCR (BK7 glass) are 1.513, and the dichroic mirror (fused silica) is 1.456.

Vertical Distances:(referenced to the atoms)	
Component	**Optical Distance (cm)**
Center of upper cage cube (OSG layer height, 90° turning mirror)	35.42
Bottom of upper cage cube (1" above bottom cage cube top)	33.44
Top of lower cage cube	30.90
Lower Cage Cube Center (Polarization layer height, flipper mirror)	28.92
Top of L-bracket (3" above breadboard)	26.51
LCR	22.79
Dichroic	18.16
f=300mm Lens	14.96
Chamber Window	3.96
Atoms	0.00
Horizontal Distances: Polarization Layer	
Fiber to flipper mirror	25.5
1m Lens	25.3
Fiber to atoms	54.4

Table A.4: Optical distances to various components referenced to the atom location. Horizontal distances are along the direction of propagation of the laser, and assume fiber is plugged into the mount that passes the beam straight through the PBS.

Horizontal Distances (cm): OSG Layer	
Fiber to 90° turning mirror	14.8
400mm Lens, from fiber	11.6
Fiber to atoms	50.2

Table A.5: Optical distances to various OSG layer components. Horizontal distances are along the direction of propagation of the laser.

A.3 Blow-Away Machine Parts Drawings

Angle Adapter

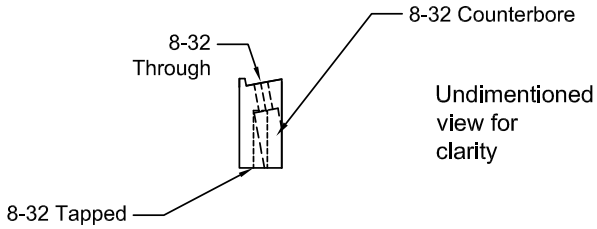

Undimentioned
view for
clarity

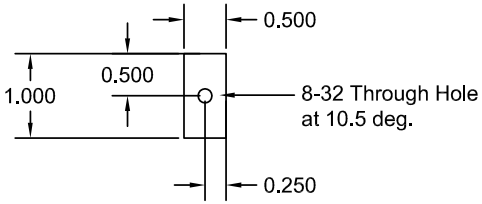

Top View

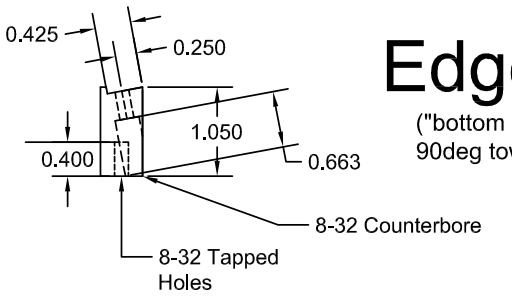

Edge View

("bottom view" rotated
90deg toward reader)

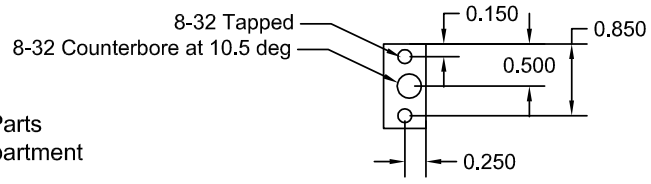

Bottom View

Joshua Hill
461 Blow Away Beam Parts
Killian Lab: Physics Department
Dimensions in inches
All tolerances: ±0.01" unless otherwise specified
Material: Aluminum
09/2016

Chamber Mount

Side View

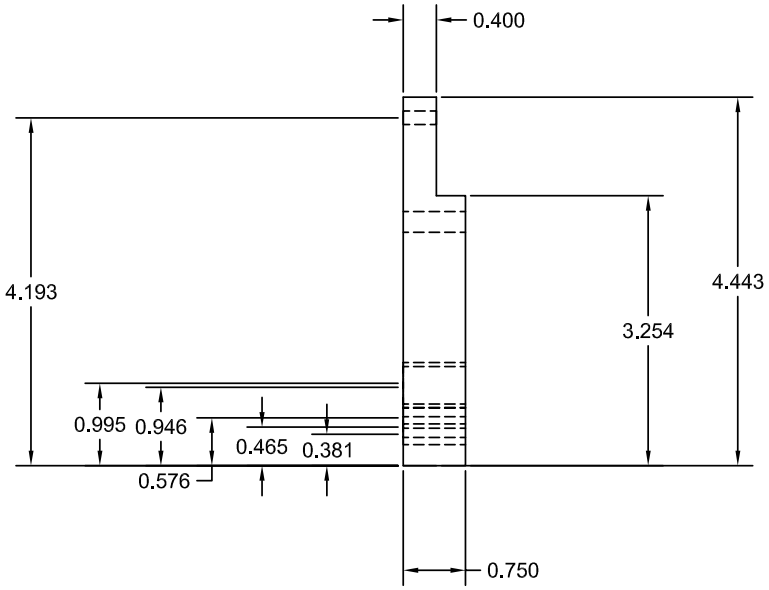

Top View

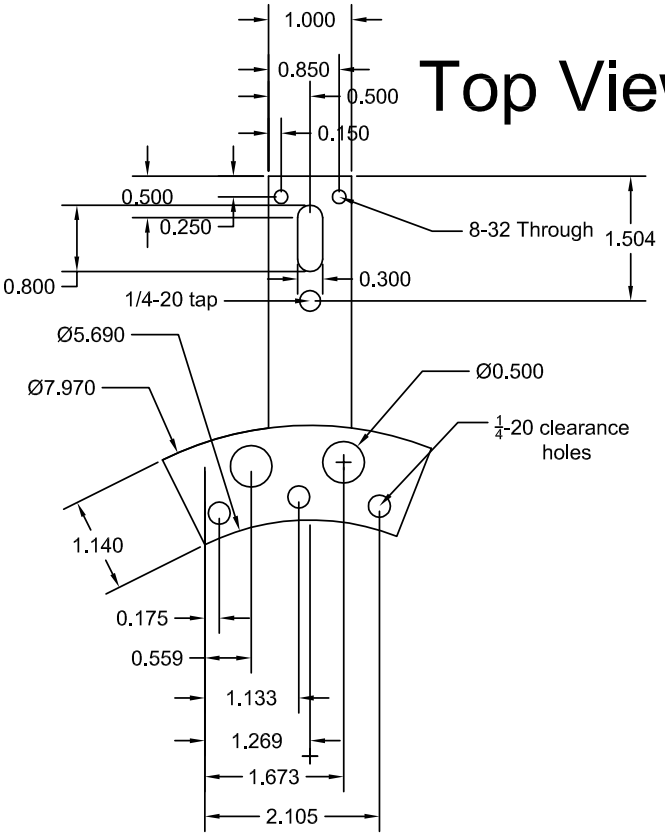

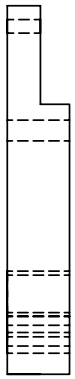

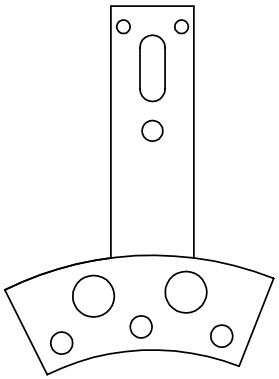

Undimentioned view for clarity

Joshua Hill
461 Blow Away Beam Parts
Killian Lab: Physics Department
Dimensions in inches
All tolerances: ±0.01" unless otherwise specified
Material: Aluminum
09/2016

A□M Adapter for Thorlabs PY005

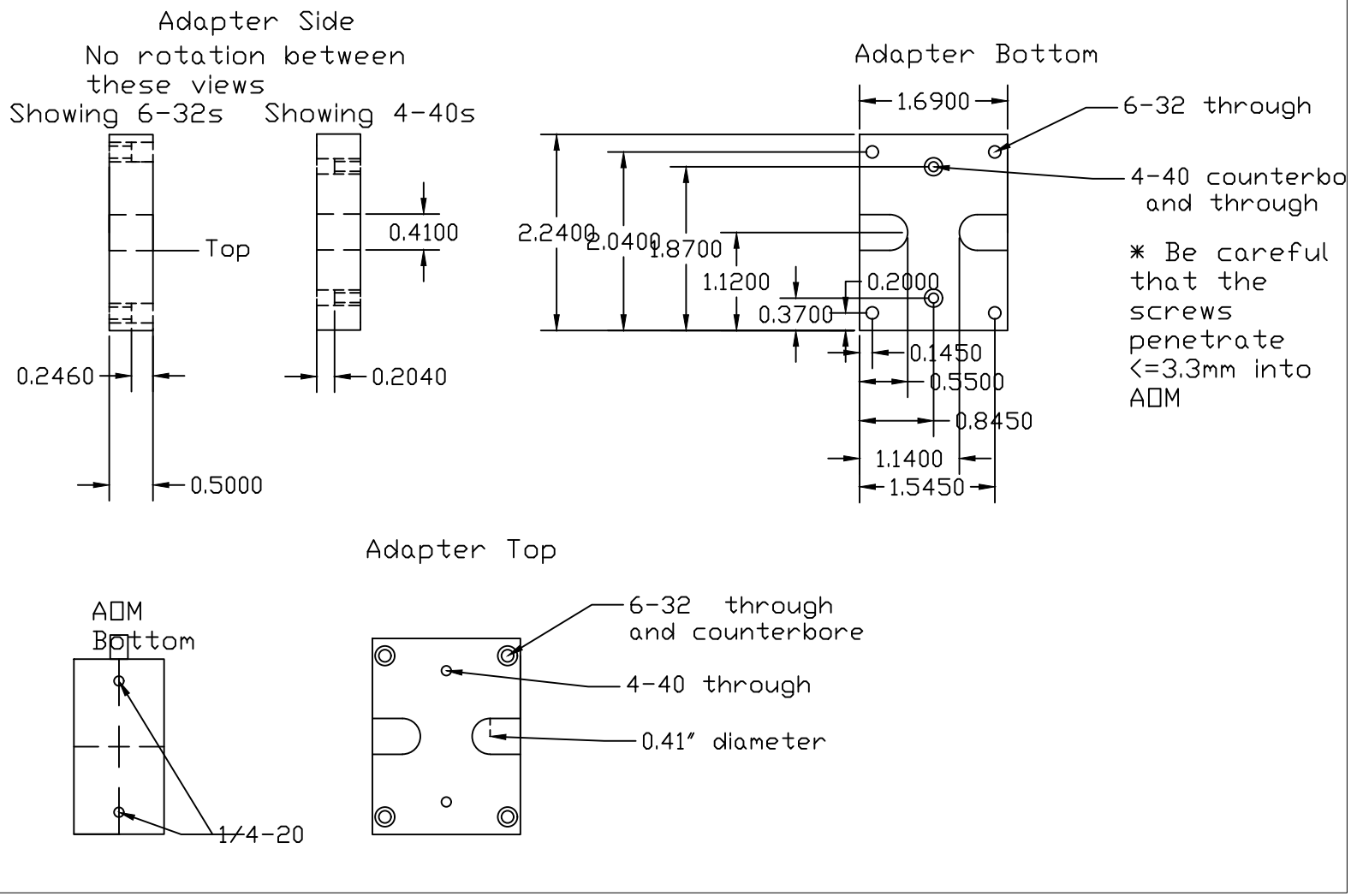

A.4 Optical Pumping and OSG Machine Parts Drawings

REVISIONS				
ZONE	REV	DESCRIPTION	DATE	APPROVED

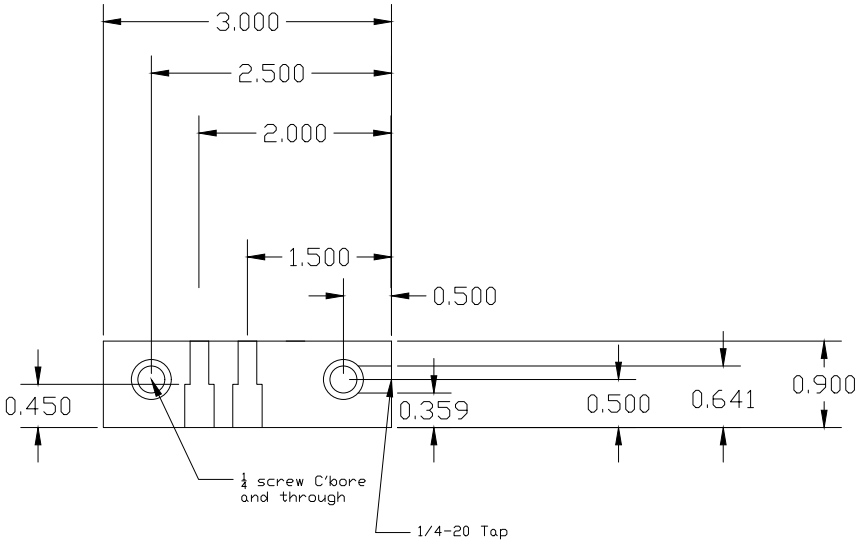

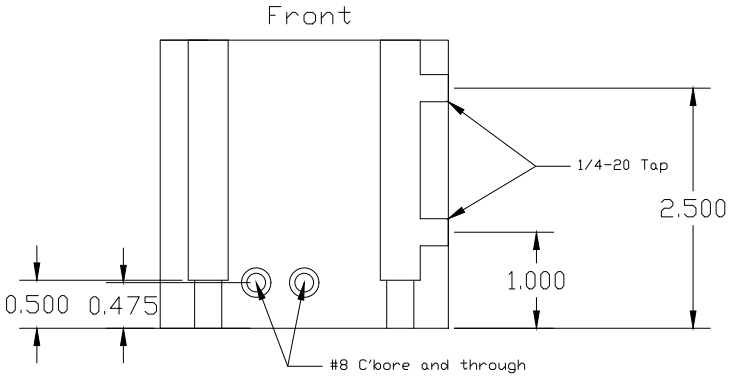

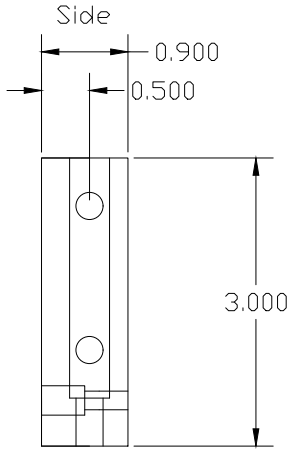

FILE NAME Block_1.dwg	L Bracket Block 1 Killian Lab Neutral Expt.		
CONTRACT NO			
DRAWN 4/19/2017	Quantity:1 Aluminum		
CHECK			
APPR.			
ISSUED			
	SIZE –	FSCM NO	DWG NO / REV
	SCALE 1:1	WEIGHT	SHEET ####

REVISIONS				
ZONE	REV	DESCRIPTION	DATE	APPROVED

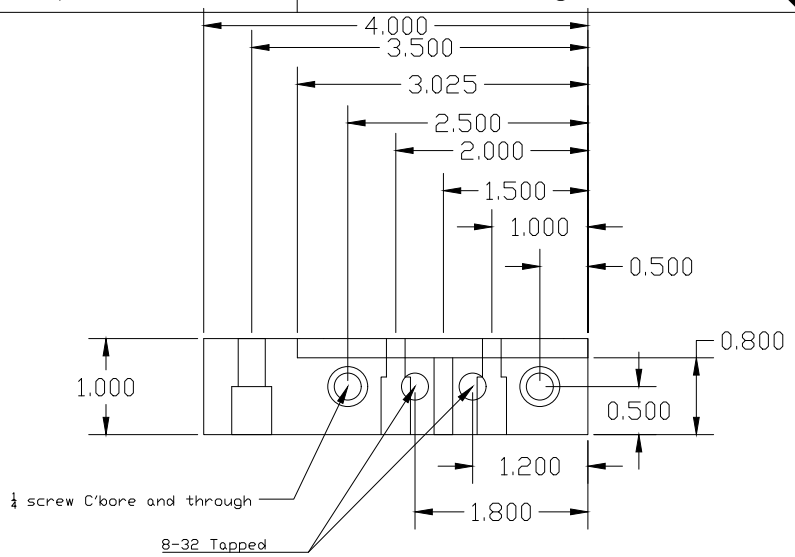

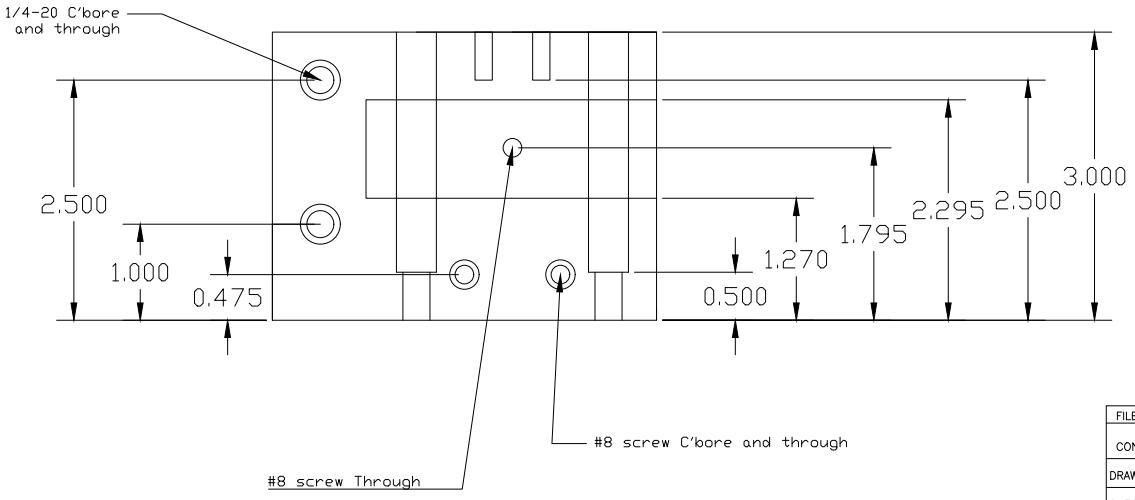

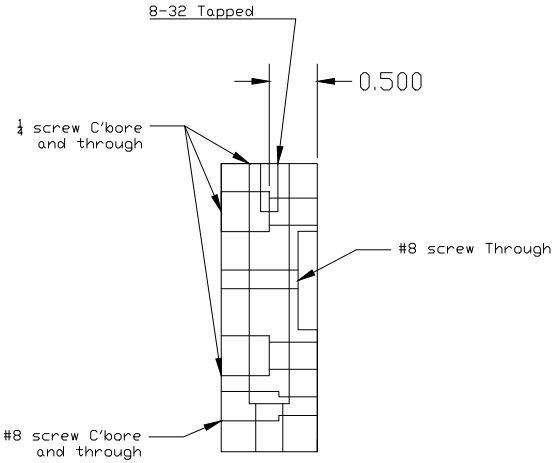

FILE NAME Block_2.dwg	L Bracket Block 2 Killian Lab Neutral Expt.		
CONTRACT NO			
DRAWN 4/19/2017	Quantity:1 Aluminum		
CHECK			
APPR.			
ISSUED			
	SIZE –	FSCM NO	DWG NO / REV
	SCALE 1:1	WEIGHT	SHEET ####

REVISIONS				
ZONE	REV	DESCRIPTION	DATE	APPROVED

In-Situ

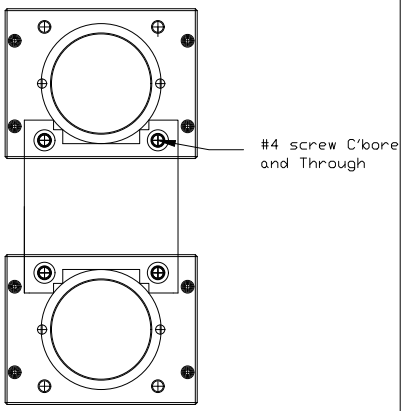

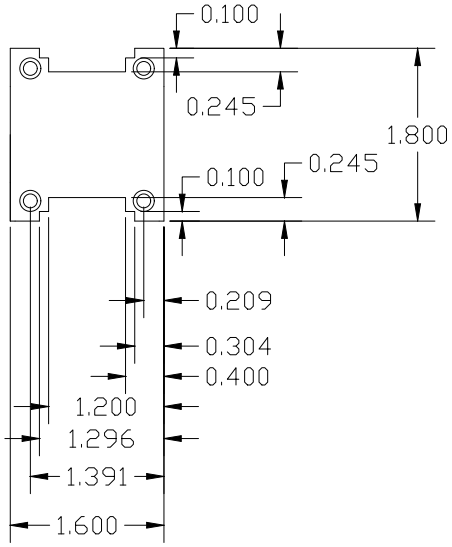

Note to users:Made to work with $\frac{3}{8}$" long 4-40 screws

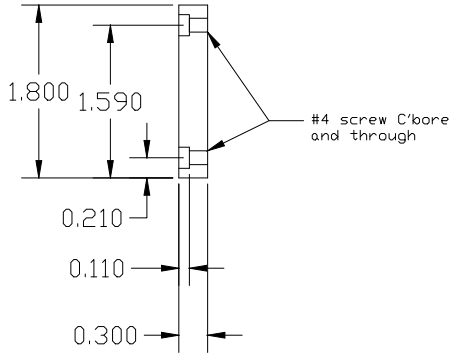

FILE NAME Cube Connector.dwg	C6W Cube Connector Plate Killian Lab Neutral Expt.		
CONTRACT NO			
DRAWN 4/19/2017	Quantity: 2 Aluminum		
CHECK			
APPR.			
ISSUED			
	SIZE –	FSCM NO	DWG NO / REV
	SCALE 1:1	WEIGHT	SHEET ####

REVISIONS				
ZONE	REV	DESCRIPTION	DATE	APPROVED

Top

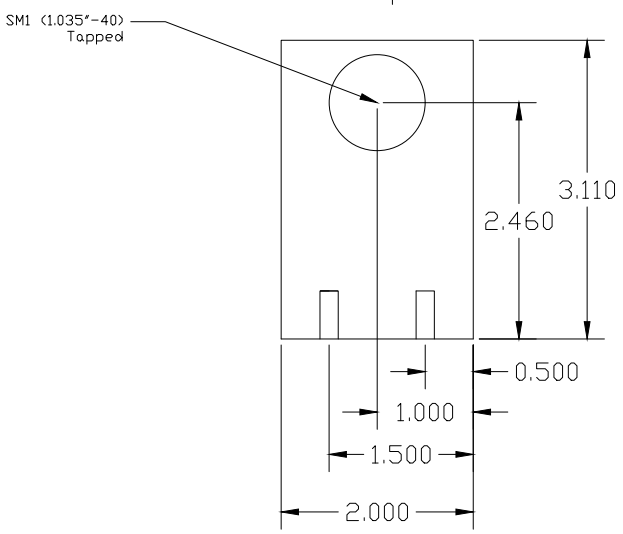

Front View

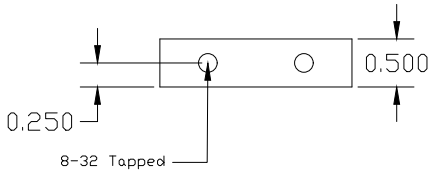

Side

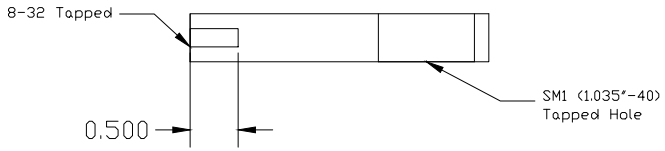

FILE NAME Detach Lens Mount.dwg	Detachable Lens Mount Killian Lab Neutral Expt.		
CONTRACT NO			
DRAWN 4/19/2017	Quantity:1 Aluminum		
CHECK			
APPR.			
ISSUED			
	SIZE –	FSCM NO	DWG NO / REV
	SCALE 1:1	WEIGHT	SHEET ####

REVISIONS				
ZONE	REV	DESCRIPTION	DATE	APPROVED

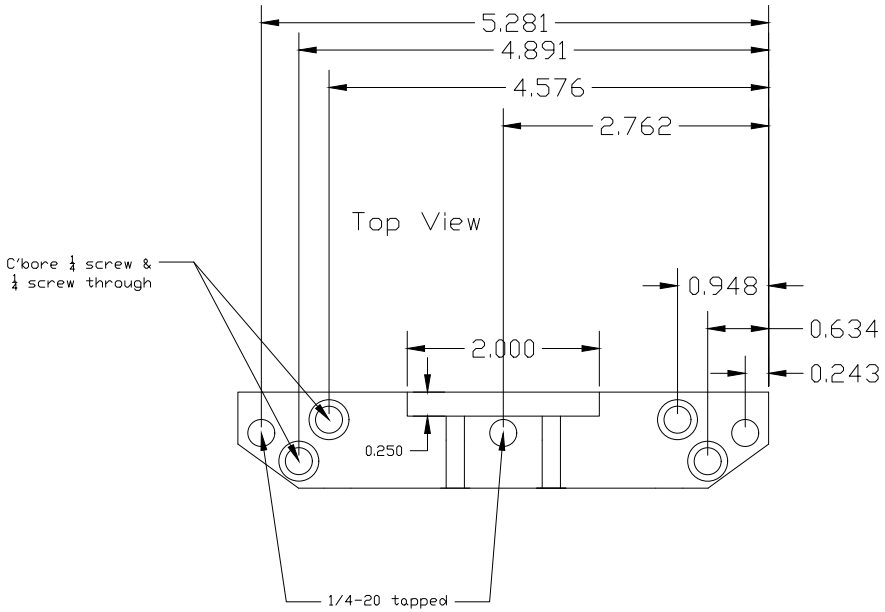

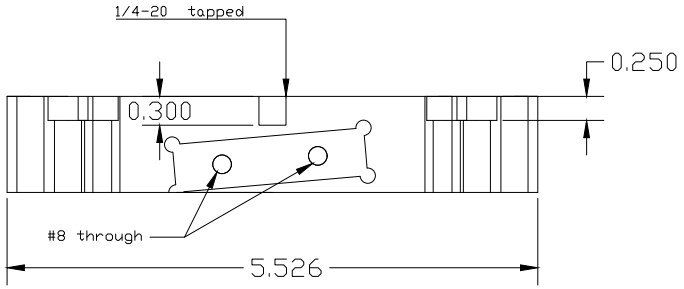

Lengthwise (Side) View

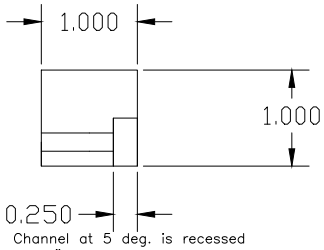

Channel at 5 deg. is recessed 0.250"

Details for the 5 deg. recess

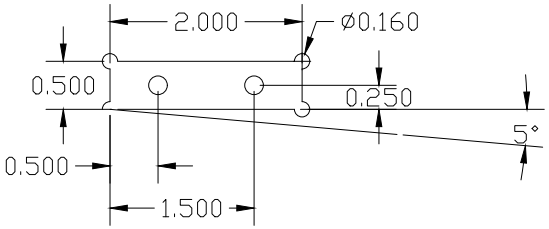

FILE NAME Lens Bar.dwg	Lens Bar Killian Lab Neutral Expt.		
CONTRACT NO			
DRAWN 4/19/2017	Quantity: 1 Aluminum		
CHECK			
APPR.			
ISSUED	SIZE –	FSCM NO	DWG NO / REV
	SCALE 1:1	WEIGHT	SHEET ####

REVISIONS				
ZONE	REV	DESCRIPTION	DATE	APPROVED

Top View

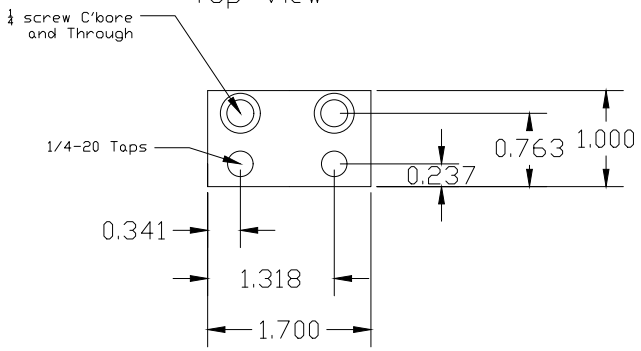

Side View

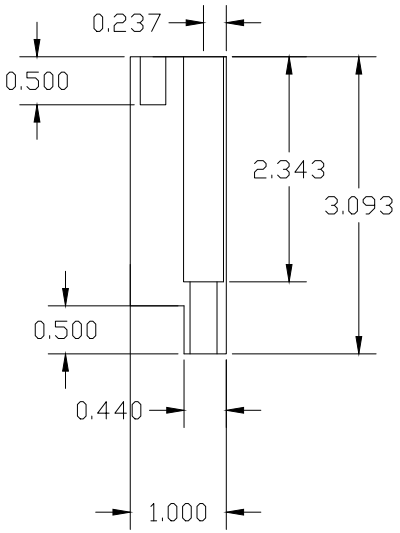

Front View

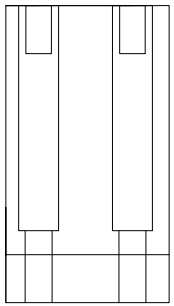

FILE NAME Long Pillar.dwg	Killian Lab: Neutral Expt. Long Chamber Pillar: Aluminum		
CONTRACT NO			
DRAWN 4/19/2017	Quantity: 1		
CHECK			
APPR.			
ISSUED			
	SIZE – / FSCM NO	DWG NO	REV
	SCALE 1:1	WEIGHT	SHEET ####

REVISIONS				
ZONE	REV	DESCRIPTION	DATE	APPROVED

Top View

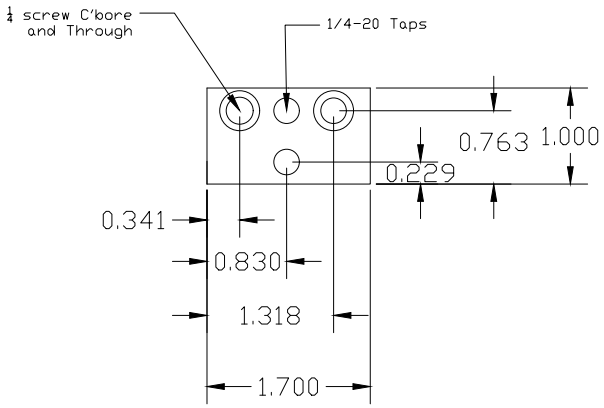

Side View

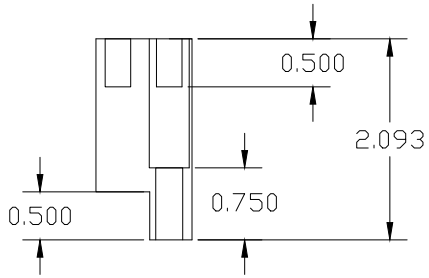

Front View

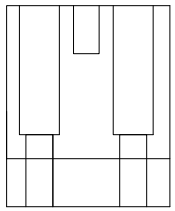

FILE NAME Short Pillar.dwg	Short Chamber Pillar Killian Lab Neutral Expt.		
CONTRACT NO			
DRAWN 4/19/2017	Quantity: 2 Aluminum		
CHECK			
APPR.			
ISSUED			
	SIZE –	FSCM NO	DWG NO / REV
	SCALE 1:1	WEIGHT	SHEET ####

Mount for Thorlabs MMF101 Motorized Flipper

Top Down View

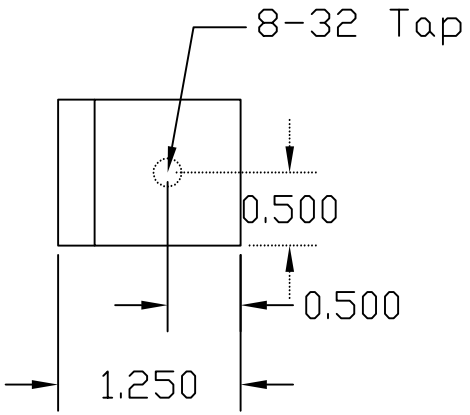

Front View

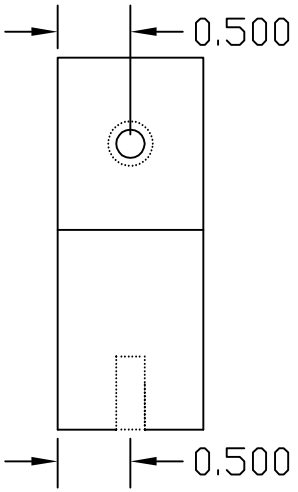
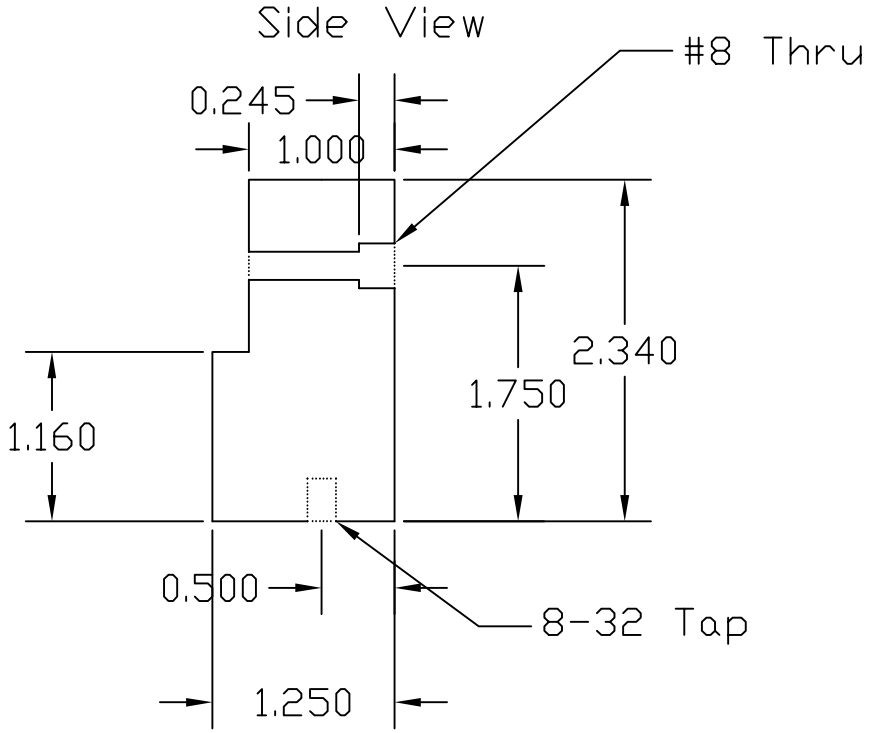
Side View